



HAL
open science

How Ammonium Valeric Acid Iodide Additive Can Lead to More Efficient and Stable Carbon-Based Perovskite Solar Cells: Role of Microstructure and Interfaces?

Lara Perrin, Emilie Planes, Takaya Shioki, Ryuki Tsuji, Jean-claude Honore, Cynthia Farha, Seigo Ito, Lionel Flandin

► To cite this version:

Lara Perrin, Emilie Planes, Takaya Shioki, Ryuki Tsuji, Jean-claude Honore, et al.. How Ammonium Valeric Acid Iodide Additive Can Lead to More Efficient and Stable Carbon-Based Perovskite Solar Cells: Role of Microstructure and Interfaces?. Solar RRL, 2024, 10.1002/solr.202400393. hal-04679689

HAL Id: hal-04679689

<https://hal.science/hal-04679689v1>

Submitted on 28 Aug 2024

HAL is a multi-disciplinary open access archive for the deposit and dissemination of scientific research documents, whether they are published or not. The documents may come from teaching and research institutions in France or abroad, or from public or private research centers.

L'archive ouverte pluridisciplinaire **HAL**, est destinée au dépôt et à la diffusion de documents scientifiques de niveau recherche, publiés ou non, émanant des établissements d'enseignement et de recherche français ou étrangers, des laboratoires publics ou privés.



Distributed under a Creative Commons Attribution - NonCommercial - NoDerivatives 4.0 International License

How Ammonium Valeric Acid Iodide Additive Can Lead to More Efficient and Stable Carbon-Based Perovskite Solar Cells: Role of Microstructure and Interfaces?

Lara Perrin,* Emilie Planes, Takaya Shioki, Ryuki Tsuji, Jean-Claude Honore, Cynthia Farha, Seigo Ito, and Lionel Flandin

As perovskite photovoltaic devices can now compete with silicon technology in terms of efficiency, many strategies are investigated to improve their stability. In particular, degradation reactions can be hindered by appropriate device encapsulation, device architecture, and perovskite formulation. Mesoporous device architectures with a carbon electrode offer a plausible solution for the future commercialization of perovskite solar cells. They represent a low-cost and stable solution with high potential for large-scale production. Several studies have already demonstrated the potential of the mixed 2D/3D ammonium valeric acid iodide-based MAPbI₃ formulation to increase the lifetime of pure MAPbI₃. They can however not describe the mechanisms responsible for the lifetime improvement. Using a full set of characterization techniques in the initial state and as a function of time during damp-heat aging, new insights into the performance and degradation mechanisms may be observed. With (5-AVA)_{0.05}MA_{0.95}PbI₃, the solar cells are very stable up to 3500 h and the degradation of performances essentially results from the loss of electrical contacts mainly located at the interfaces. In contrast, for the neat MAPbI₃, a poor stability is evidenced (T₅₀ = 500 h) and the loss in performance results from the degradation of the bulk perovskite layer itself.

1. Introduction


Since the first use of perovskite materials in a photovoltaic device in 2008,^[1] the 3.8% efficiency achieved using CH₃NH₃PbI₃ crystals has now progressed up to a 26.1% record efficiency.^[2] This optimization resulted from several modifications in both the device architecture and the constitutive materials. However, several critical issues still need to be addressed before perovskite devices can be industrially scaled up, such as the lack of processes compatible with large-scale production and the low durability of performances when exposed to excess moisture, light, heat, and oxygen. Today, most perovskite solar devices exhibit poor duration in real usage conditions, in the range of days to weeks without encapsulation. This is mainly due to the degradation of the perovskite layer caused by a combination of the environmental factors. Recently, many strategies have been proposed to improve the stability, in particular, the degradation reactions can be partially limited by proper

device encapsulation, device architecture, and choice of perovskite formulation. First, the use of an efficient encapsulation is mandatory to achieve a reasonable lifetime in the damp-heat-normalized test (85 °C/85% relative humidity [RH]). The main encapsulation concept commonly used for an effective protection of perovskite photovoltaic devices is as follows: glass–glass encapsulation using a thermoplastic hot-melt pressure-sensitive sealing material.^[3] But, the stability should also be optimized through the selection of the devices' architectures.

Mesoporous device architectures using a carbon electrode provide a stable solution for the future commercialization of perovskite solar cells (PSCs).^[4] These devices consist of three stable mesoporous layers (TiO₂, ZrO₂, and carbon) which are infiltrated with a perovskite solution at the very end of the entire protocol. This architecture even operates without a hole-transporting layer due to the carbon electrodes' ability to extract photogenerated holes, thus avoiding the need for the commonly used expensive and unstable organic hole-transporting layers.^[5] The use of carbon electrodes also avoids the formation of metal halides observed when using traditional metal electrodes with

L. Perrin, E. Planes, J.-C. Honore, C. Farha, L. Flandin
University Grenoble Alpes
University Savoie Mont Blanc
CNRS, Grenoble INP, LEPMI
38000 Grenoble, France
E-mail: lara.perrin@univ-smb.fr

T. Shioki, R. Tsuji, S. Ito
University Hyogo, Department of Materials and Synchrotron Radiation
Engineering
Graduate School of Engineering
Shosha, Himeji, Hyogo 2167, Japan

 The ORCID identification number(s) for the author(s) of this article can be found under <https://doi.org/10.1002/solr.202400393>.

© 2024 The Author(s). Solar RRL published by Wiley-VCH GmbH. This is an open access article under the terms of the Creative Commons Attribution-NonCommercial-NoDerivs License, which permits use and distribution in any medium, provided the original work is properly cited, the use is non-commercial and no modifications or adaptations are made.

DOI: 10.1002/solr.202400393

perovskite.^[6] As a consequence, the sole use of carbon-based devices architecture increases the durability of the PSCs.^[7] Even the common $\text{CH}_3\text{NH}_3\text{PbI}_3$ perovskite has demonstrated 4500 h of stability under thermal stress at 100 °C using such devices.^[8] The triple-mesoscopic carbon-based perovskite device architecture (FTO glass/compact TiO_2 /mesoporous TiO_2 /mesoporous ZrO_2 /mesoporous carbon) was first introduced in 2013.^[9] It represents a low-cost and stable solution with high potential for large-scale production. In fact, the entire device fabrication process can be carried out under ambient atmosphere, because the sensitive perovskite material is incorporated at the end of the process, minimizing its manipulation and degradation. Furthermore, all layers can be processed using scalable techniques compatible with large-scale and large-area production: screen, inkjet, or spray printing methods for the TiO_2 / ZrO_2 /carbon scaffold and automated drop-casting or inkjet printing for the perovskite precursors solution infiltrating the mesoporous scaffold. To date, rules have even been established for the formulation of carbon electrodes to allow perfect permeability into the underlying TiO_2 / ZrO_2 porous layers.^[10,11] Triple-mesoscopic carbon-based perovskite device architecture could thus be considered as the most suitable choice for its easy adaptability in a possible pilot line production. However, despite their excellent stability, lower efficiency than metal-based devices is generally reported mainly attributed to weak charge transfer at the interfaces. Such carbon-based perovskite devices have however recently achieved a record power conversion efficiency (PCE) of 22.2%,^[12] which is largely competitive with traditional n-i-p or p-i-n perovskite devices using metallic electrodes or multicrystalline silicon records, sweeping challenges in scaling up.^[13] They have even demonstrated their potential for easy recycling and possible reuse of the mesoporous framework.^[14]

Regarding the stability issue of the perovskite layer itself, lower-dimensional (2D) perovskite structures have been identified for their thermal robustness and higher resistance to moisture compared to the traditional 3D counterparts.^[15,16] Their photovoltaic properties and improved moisture stability were first reported in 2014,^[17] but more general optoelectronic properties such as a wider optical bandgap and a higher exciton binding energy overshadow these attractive features and penalize the PCE. It wasn't long before researchers began exploring mixed dimensional 2D/3D hybrid perovskite,^[18] expected to combine the benefits of the two individual systems, and thereby offering a great potential for the future of PSCs.^[16] Among the various large cations tested for 2D doping of 3D perovskite structures,^[19–21] the 5-ammonium valeric acid (AVA) has demonstrated significant enhancement in both efficiency and durability within the aforementioned carbon-based mesoscopic architecture.^[22,23] In such devices, the mixed 2D/3D perovskite obtained with the addition of 5-ammonium valeric acid iodide (AVAI = $\text{HOOC}(\text{CH}_2)_4\text{NH}_3\text{I}$) to the traditional $\text{CH}_3\text{NH}_3\text{PbI}_3$ formulation has already demonstrated a shelf-life stability of over 1 year without encapsulation (in the dark, under ambient atmospheric conditions).^[24] Under continuous illumination, the use of this AVAI-based 2D/3D perovskite compared to the standard 3D $\text{CH}_3\text{NH}_3\text{PbI}_3$ allows to better maintain the performances both in traditional devices with metallic electrodes (70% after 300 h for 2D/3D, against 50% for 3D)^[22] and in carbon-based devices (100% stable after 10 000 h for 2D/3D, against 50% after

250 h for 3D),^[22,25] demonstrating a strong benefit of this formulation for carbon-based devices. Under 85 °C/85% RH aging conditions (in the dark), previous AVAI-based 2D/3D perovskite already demonstrated a stability over 3000 h in carbon-based devices against 50% after 250 h for 3D $\text{CH}_3\text{NH}_3\text{PbI}_3$ or even worth for 3D $\text{Cs}_{0.1}\text{FA}_{0.9}\text{PbI}_3$ perovskite showing nonperforming devices after 100 h.^[25,26] The 5-AVA moiety possesses bifunctional end groups (ammonium and carboxyl). This could favor effective coordination with MAPbI_3 perovskite due to the AVA ability for Lewis acid–base coordination and hydrogen bonding interactions, resulting in longer durability and moisture resistance together with lower-defect formation.^[23,27–29] It has also been reported in the literature that AVAI even improves the mechanical stability of the perovskite film. This was also attributed to its bifunctional end groups that can link perovskite grains closely to resist cracks formation.^[30] To recapitulate the potential of the AVAI-based MAPbI_3 formulation in carbon-based devices, it is pertinent to note that the literature^[25] already highlights that they are able to pass the key international electrotechnical commission (IEC)61 215 standards needed for photovoltaic (PV) commercialization:^[31] damp-heat (85 °C/85% RH, 1000 h), thermal cycling (−40 °C/85 °C, 200 cycles), UV preconditioning (60 °C, 50 kWh m^{−2}, higher than the 15 kWh m^{−2} IEC requirement), and maximum power point tracking under illumination (55 ± 5 °C, 1000 h). The performance of AVAI-based MAPbI_3 device was not significantly affected by any of these tests, while its pure MAPbI_3 counterpart showed a notable decrease in PCE.

The present study aims to highlight the differences in the behavior of carbon-based mesoscopic perovskite devices based on the traditional MAPbI_3 perovskite (MA = CH_3NH_3) when prepared with or without the addition of 5-AVAI. Identical procedures for precursor solutions, infiltration, and curing were used for both perovskite formulations. A study of the mechanisms occurring will be carried out using a full set of characterization techniques including macroscopic photovoltaic measurements, light-beam-induced current (LBIC) imaging, photoluminescence (PL) spectroscopy and imaging, UV–visible reflection–absorption spectroscopy, X-ray diffraction (XRD), and impedance spectroscopy. This will be carried out both at the initial state and during damp-heat aging to provide new insights into the performance and degradation mechanisms of carbon-based mesoscopic PSCs. In addition, a special attention will be given to the method used to measure performance by analyzing the current-voltage $J(V)$ curves at different scan rates. Indeed, the literature on perovskite photovoltaics sometimes mentions a dependence of the $J(V)$ characteristics on the voltage scan rate, transient phenomena, or hysteresis behaviors, which were initially interpreted as capacitive effects.^[17,32] However, we have recently proposed a novel electrical equivalent circuit that allows the modeling of typical observed behaviors in devices such as those studied here.^[33] It consists of two standard one-diode models, one is transient and the other permanent. The observed behavior was interpreted as a structural relaxation between two extreme states, and the characteristic time is consistent with the timescales typically associated with large charge carriers, such as large ions. Another recent paper^[34] published in the same period also reveals the complex interplay between ionic and electronic charges in such device architectures, and supports the argument that the previously mentioned differences observed in $J(V)$

pattern are induced by organic cation migration, as it can be suppressed using a fully inorganic perovskite formulation.

Several studies already highlight the potential of AVAI-based MAPbI₃ formulation to exceed the durability of pure MAPbI₃ perovskite.^[22,25] According to literature cost analysis of such devices, the AVAI doping proposed approach even presents a high economic feasibility with only an additional cost of 1.63% for raw materials and without any additional manufacturing step.^[35] However, damp-heat comparative aging studies are usually conducted on relatively short duration (≤ 1000 h, which is the IEC 61215 requirement for silicon devices) and very few of them are coupled with a study of the mechanisms involved in the difference of lifetime between (5-AVA)_xMA_{1-x}PbI₃ and MAPbI₃ perovskites. In addition, to the best of our knowledge, no other publication reports the monitoring during 3500 h of photovoltaic parameters according to different $J(V)$ measurements conditions.

2. Results and Discussion

Figure 1a illustrates the architecture of studied C-PSCs, together with the energy diagram of its constituting layers. A typical C-PSC comprises a front FTO/glass substrate, a mesoporous electron-transporting layer, an insulating intermediate layer, and finally a mesoporous carbon electrode.^[2] As previously demonstrated,^[3] the method of perovskite deposition and the quantity of perovskite infiltrated into these devices play a crucial role in their stability. While the drop-casting infiltration method may have less potential in terms of deposit homogeneity compared to inkjet printing, it has demonstrated to produce highly stable devices.^[3] The amount of perovskite that can be infiltrated by inkjet-printing is limited by the volume of each injection, which must not dissolve neighboring perovskite crystals risking degradation of the PCE, and by the potential crystallization in the printer nozzle if the perovskite solution is too concentrated. As the main advantage of C-PSC lies in the use of a mesoporous skeleton which can act as a “reservoir” for the active layer material,^[36] the drop-casting technique provides greater flexibility in controlling the amount of perovskite injected and was therefore selected in this study.

In this study, two perovskite formulations were compared: MAPbI₃ and (5-AVA)_xMA_{1-x}PbI₃. However, to avoid potential defects in the middle of devices, the drop-casting infiltration was carefully conducted on one edge of the mesoporous scaffold. The goal was to underline the differences in behavior between C-PSC devices based on the traditional MAPbI₃ perovskite when fabricated with or without the addition of 5-AVAI. The star diagram in Figure 1b presents the PV parameters obtained at initial state (average values and standard deviations are also given in Table S1, Supporting Information). Obtained values are in accordance with state-of-the-art data corresponding to such carbon-based devices using a simple process with minimal manufacturing steps all conducted under ambient atmosphere to be compatible with a scaling-up perspective (see Table S2, Supporting Information).

The $J(V)$ curve pattern demonstrates a dependency on the voltage scanning speed; hence, PV parameters are given for the two observed boundaries. Figure 1c highlights the significant variations observed for devices based on the perovskite formulation

with AVAI, showing a “bump” pattern at intermediate scan speeds and a consistent curve pattern at both boundaries located at 1 mV s⁻¹ for the lowest curve and 500 mV s⁻¹ for the highest curve. The lowest curve reflects the actual operating conditions, as halting the scan rate while maintaining the voltage bias during the highest curve results in the current returning to the value of the lowest curve. As previously reported, investigated, and modelled,^[33] this unconventional behavior is due to a relaxation mechanism independent of the photovoltaic effect, suggesting a diffusion mechanism. It could be also mentioned that it occurs whatever the illumination intensity, as already demonstrated for 0.2 sun.^[33]

Both boundaries set of PV parameters (at 1 and 500 mV s⁻¹) are of interest, as it sounds theoretically possible to prevent this ion diffusion and thus interfacial contamination, ultimately stabilizing the photocurrent to the value obtained at the highest boundary. Intermediate curves showing a “bump” pattern should not be considered for PV parameters determination. It could for instance lead to inaccurate FF values (possibly higher than 100%). The FF values obtained at boundaries are appropriate and both in the 57–67% range.

Regarding the formulation without AVAI (Figure 1d), the phenomenon is less pronounced compared to AVAI-based devices, but it remains present. The amplitudes of the relaxation (J_{sc} difference) are respectively 9.8 ± 0.6 and 2.2 ± 0.7 mA cm⁻² for perovskites with and without AVAI. In addition, as the voltage at the inflection point shows a linear correlation with the scan rate, it is possible to access to the related characteristic relaxation times,^[33] which are respectively 23.2 ± 4.4 and 4.1 ± 0.3 s for perovskites with and without AVAI. Such values are in good alignment with the order of magnitude of large charge carriers, such as large cations migration as found in our previous work.^[33] The difference in relaxation time for the two systems here studied is consistent with the size difference between AVA and MA cations, possessing molar masses of 118 and 32 g mol⁻¹, respectively.

Furthermore, superior performances were observed for (5-AVA)_xMA_{1-x}PbI₃ with PCE values of $12.1 \pm 0.8\%$ and $8.4 \pm 0.7\%$ for respectively the so-called “metastable” (high scan rate) and “stable” (low scan rate) states, compared to MAPbI₃ with PCE of respectively $5.4 \pm 1.1\%$ and $3.9 \pm 0.7\%$. This increase in PCE by adding AVAI in the perovskite formulation is in accordance with literature data for mesoscopic PSCs^[18] and highlights its significance in enhancing C-PSC device performance. It is noteworthy that the impact of both formulation and scan speed on PCE is similar for J_{sc} and series conductance ($1/R_s$), with the V_{oc} also found to be higher for the formulation with AVAI.

The overall PCE provides an average assessment of photovoltaic cells. Nevertheless, processing conditions might lead to variations in performance across the device’s surface. LBIC mapping serves as a suitable method to explore these variations. Figure 1e displays typical mappings obtained from our devices accompanied by violin plots representing the current distribution across the entire active area. Both the violin plots and the raw LBIC maps reveal higher local I_{sc} for devices containing AVAI, consistent with the macroscopic PCE and J_{sc} values. The current mappings exhibit a relatively uniform distribution. However, the infiltration location of the perovskite precursors’ solution is clearly visible at the top center of the photoactive layers. In addition, the formulation without AVAI is less active in the corner areas.

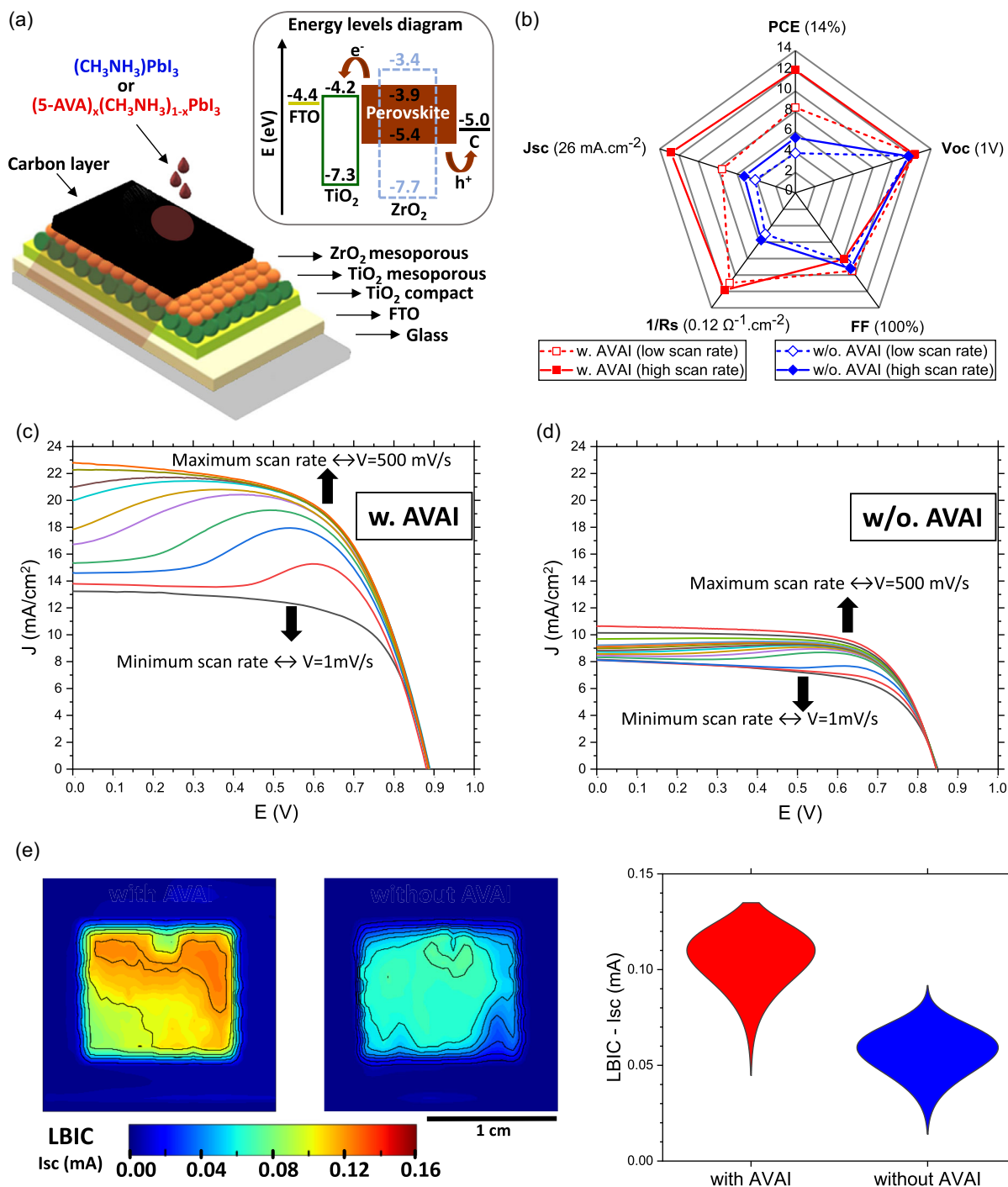


Figure 1. a) C-PSC cell architecture with a simplified representation of the edge drop-casting perovskite deposition process here used (inset: energy levels diagram of the different layers); b) star diagram representing PV parameters for the two studied perovskite formulations (average on a 5 cells batch for each) measured using either 1 mV s⁻¹ for low scan rate (empty symbols and dotted lines) and 500 mV s⁻¹ for high scan rate (full symbols and full lines); c, d) J(V) measurements performed at different scan rates for C-PSCs with respectively (5-AVA)_xMA_{1-x}PbI₃ (with AVAI) or MAPbI₃ (without AVAI) perovskite formulations (in reverse scan); and e) LBIC maps of both studied C-PSCs (the color scale represents the I_{sc} variation, same scale bar was used for both images) and statistical representation under violin plots of LBIC maps homogeneity over the full active area of cells.

Figure 2 presents additional characterizations, focusing on perovskite material, aiming to elucidate the differences observed in PV performances between the two formulations. To delve

deeper into the investigation of AVAI's impact, UV-visible spectroscopy was initially employed. However, performing fully informative analyses using this technique proved challenging.

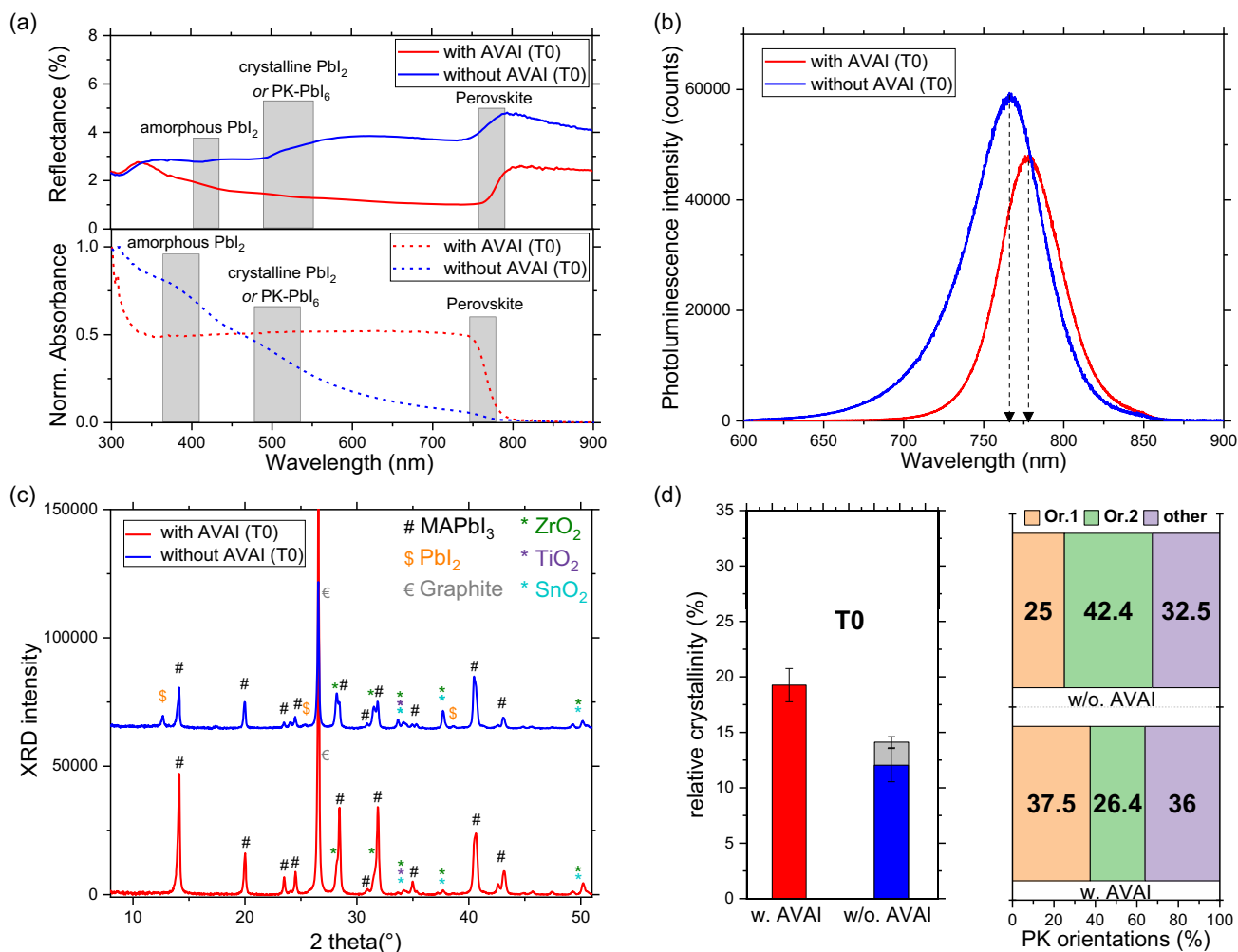


Figure 2. For devices formulated with and without AVAI: a) UV–visible reflectance spectra (performed on complete cells from FTO side) and absorbance spectra (performed on cells after CL removal); b) photoluminescence spectra (on complete cells from FTO side); c) XRD diffractograms with main diffraction lines assignment (after CL removal); and d) XRD relative crystallinity of perovskite (color) and PbI_2 (grey), and orientation proportions of the perovskite (see Table S3, Supporting Information, for the attribution).

Reflectance spectra can be obtained from the glass/FTO side without opening the cells (see Figure 2a top), but this method is less sensitive than absorbance spectra. Absorbance spectra were hindered by the presence of an opaque carbon layer, preventing the acquisition of non-saturated spectrum. To address this issue, previous studies^[18,22,23] often present absorbance spectra of half-devices fabricated without the final CL. However, the CL is the thicker layer (10–12 μm) of the device architecture and it is difficult to finely adapt the volume of the perovskite precursor solution to ensure that a final perovskite layer is contained only within the mesoporous $\text{TiO}_2 + \text{ZrO}_2$ backbone, without any upper compact perovskite layer. Moreover, it was recently demonstrated that the CL also protect the photovoltaic devices during aging by delaying and homogenizing the moisture diffusion toward the perovskite layer.^[37] As presented in previous works,^[38] full devices are monitored and absorbance spectra were recorded after removal of the CL (see Figure 2a bottom), achieved using an adhesive scotch

peeling method which is destructive for the solar cell. As this method could potentially remove a small quantity of the perovskite layer, the presented spectra are normalized to account for any such effects.

UV–visible reflectance and absorbance spectra both present a transition around 780 nm, characteristic of the 3D phase for MAPbI_3 perovskite. Utilizing the Tauc plot method, an optical bandgap of exactly 1.58 eV was determined for both perovskite formulations (see Figure S1, Supporting Information, for Tauc plots applied to reflectance spectra using the Kubelka–Munk^[39] function). For the formulation with AVAI, no contribution for a pure 2D AVAI-based perovskite phase was observed (AVA_2PbI_4 around 400–450 nm),^[22] implying a good intercalation within the 3D perovskite. For the formulation without AVAI, two additional transitions were observed, around 400 and 500 nm. These transitions could correspond to the presence of PbI_2 in its amorphous form around 400 nm and in its crystalline form around 500 nm.^[40] However, a transition around

500 nm is also referenced for perovskite itself, originating from the lead–iodide octahedra present in both MAPbI₃ and PbI₂.^[41] As the observed transition is broad in the case of the MAPbI₃ formulation without AVAI (from 490 to 600 nm, clearly visible on the reflectance spectrum, blue color), it likely contains contributions from both PbI₂ and perovskite. The perovskite–PbI₆ transition could vary in intensity depending on the environment and compactness of the perovskite layer, and is evidently absent in the formulation with AVAI additive (on both reflectance and absorbance spectra, red color). In addition, the absorption pattern is notably less flat for the formulation without AVAI suggesting a more compact perovskite layer with fewer voids or holes.^[42,43] This could originate from the presence of PbI₂ around perovskite grains in the formulation without AVAI and/or potentially larger grain sizes for the formulation with AVAI. However, the reflectance levels are approximately 1% and 4% for respectively the formulation with or without AVAI, indicating a higher absorbance level for the perovskite formulation with AVAI. This trend was also observed in the absorbance spectra but may be influenced by the variability in the CL peeling process.

PL measurements were conducted on full devices from the FTO side (see Figure 2b). The observed PL signal is attributed to the major component, namely the MAPbI₃ perovskite material, and more precisely to conduction band/valence band (CB/VB) recombination. First, the PL intensity measured for cells without AVAI consistently slightly exceeded that of cells with AVAI. This discrepancy could originate from a higher quantity of defects, such as PbI₂, within the perovskite layer or at its interfaces. PL intensity is related to the radiative recombination within perovskite. To avoid unwanted carrier recombination, the non-radiative recombination should be low.^[44] It could therefore be argued that for an optimal PV device, the PL intensity should be high, indicating attenuated non-radiative recombination. However, the situation is more complex and high PL may also indicate poor electrical extraction at interfaces.^[45] The reduction in PL observed with AVAI-based perovskite is probably due to an improvement of interfaces, with a reduction in the carrier recombination rate due to better activation of the quenching effects at the interfaces.

Additionally, a redshift was noticed upon adding the AVAI additive (15 nm at λ_{max} , 50 nm at λ_{onset}). As such a shift was not observed on UV–visible data (see Figure S1, Supporting Information), it is unlikely to be associated with a significant difference in the perovskite chemical composition. Given that traditional MAPbI₃ degradation typically results in a PL blue-shift,^[36,46,47] the observed redshift can be attributed to an improvement in the crystalline microstructure of the perovskite. More precisely, it can be related to several factors such as a decrease in the quantum confinement effect,^[48,49] which could be indicative of an increase of grain size^[50] or a different phase orientation organization,^[51] or even to an atomic distortion caused by the presence of a 2D perovskite phase.^[52] The latter is very likely to occur in the mixed 2D/3D hybrid perovskite resulting of the (5-AVA)_xMA_{1-x}PbI₃ formulation.^[16] Indeed, the addition of AVAI within the perovskite formulation could result either in a progressive insertion of AVA moiety or (AVA)₂PbI₄ perovskite within the MAPbI₃ lattice. In this way, the perovskite–PbI₆ octahedral structure and the Pb–I–Pb bond

angle might be affected by the bifunctional AVA organic large cation through hydrogen bonding interactions.^[53]

Figure 2c displays XRD diffractograms, while Figure 2d shows the extracted relative crystallinity of both perovskite phases (color) and PbI₂ (grey), along with the proportions of orientations for both perovskite phases. The plane attribution of each MAPbI₃ perovskite lines (noted # in Figure 2c) is specified in Table S3, Supporting Information. The assignment of XRD lines was conducted based on literature refs. [18,38,54] and on the XRD diffractogram of the ZrO₂/TiO₂/FTO/glass device backbone without perovskite presented in Figure S2a, Supporting Information. First, only the 3D MAPbI₃ perovskite was evidenced, while the 2D AVA₂PbI₄ perovskite was not detectable, likely due to its effective insertion into the MAPbI₃ phase as reported in literature^[22] for similar introduced AVAI amounts. Subsequently, as suspected in UV–visible spectroscopy, the presence of crystalline PbI₂ was confirmed for the perovskite formulation without AVAI, whereas it was not observable with the addition of AVAI.

In our study, an identical procedure for precursor solutions, infiltration and curing was applied for both perovskite formulations to keep an objective comparison. When not using the AVAI additive, it obviously leads to the presence of PbI₂ in the mesoporous network. This PbI₂ could either be a residual precursor or a degradation by-product. According to the literature, additional steps may be required to increase the performance of pure MAPbI₃ perovskite in such C-PSC architectures, such as post-treatment by methylammonium iodide–isopropanol solution or methylamine gas.^[25,55] Both solution and gas can enter through the perovskite voids and the PbI₂ 2D-layered structure to rapidly react with residual PbI₂ and form MAPbI₃ allowing a completion of the thick perovskite layer.^[56]

As highlighted in Figure 2d, the addition of AVAI also resulted in a 60% increase in perovskite crystallinity in absolute terms (the relative crystallinity of the MAPbI₃ phase increased from ≈12% to 19.3% between the two studied formulations). In addition, even if both obtained perovskite present the same crystal planes, they are not present in the same proportions (see Figure 2d). The perovskite planes attributed to orientations 1 and 2 and others are defined in Table S3, Supporting Information. This discrepancy is attributed to the mesoporous structure of the TiO₂/ZrO₂/CL device scaffold, which allows the perovskite to crystallize in various orientations. Specifically, orientation 1 is favored when using the AVAI additive, whereas it was orientation 2 without AVAI. The primary altered plane in return is the 440 plane at $2\Theta = 40.5^\circ$ within orientation 2.

Furthermore, in addition to the previously^[20,57] demonstrated enhancement in charge extraction speed at the TiO₂ interface facilitated by AVA (due to the ability of AVA cations, via carboxylic acid groups, to be adsorbed on both TiO₂ and ZrO₂ mesoporous layers), we can also argue that UV–visible, PL, and XRD collectively indicate an improvement in the perovskite microstructure with the addition of AVAI. This improvement aligns with the overall increase in PV performance. Following this assessment of initial properties, it would be interesting to monitor them during an aging campaign. However, it seemed us appropriate to begin by detailing the entire impact of measurement conditions to better define the protocol for aging experiments. Indeed, **Figure 3** shows the strong dependence of the measuring conditions on the $J(V)$ curve pattern.

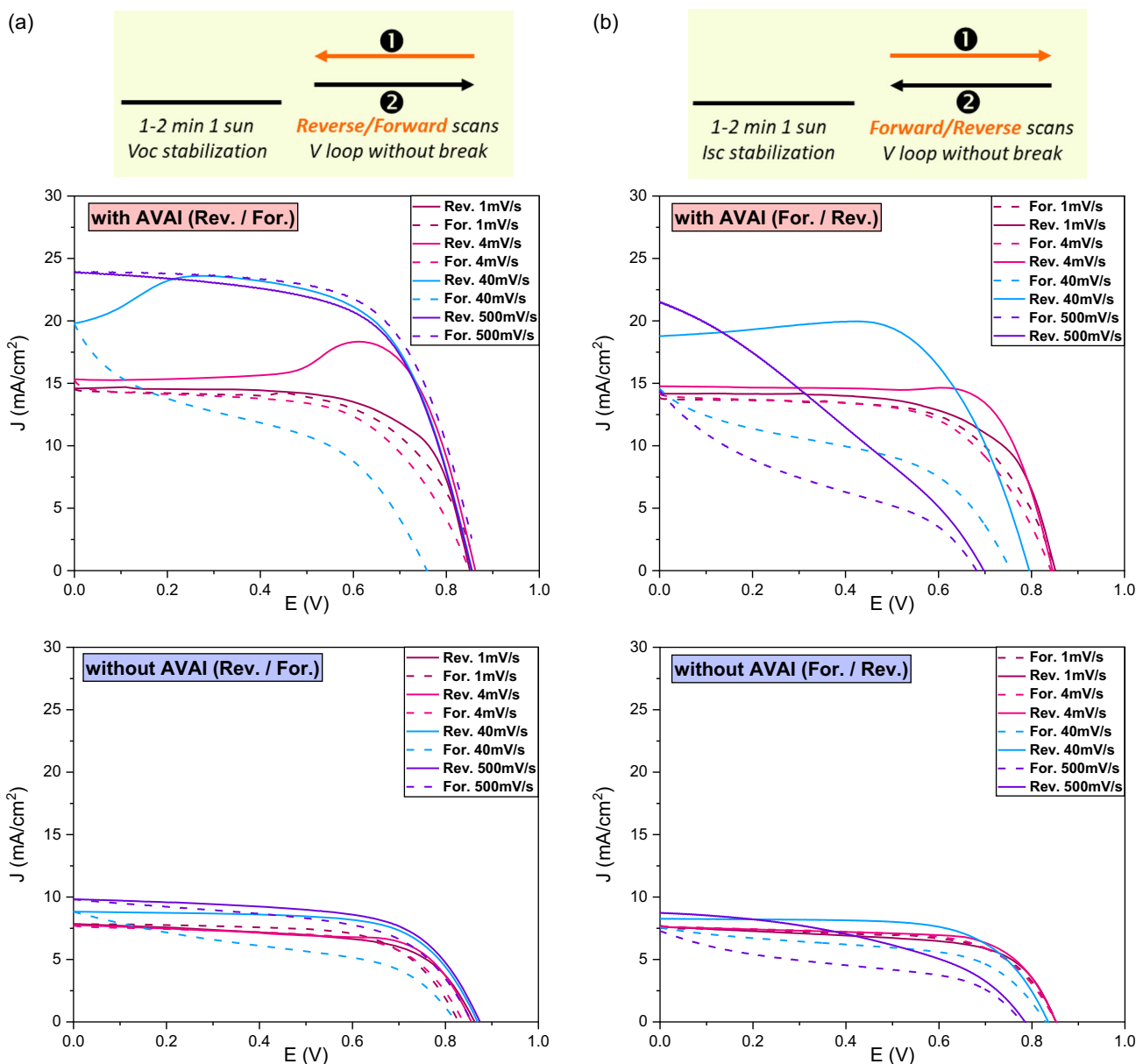


Figure 3. $J(V)$ curves (in reverse and forward voltage scan modes) at four different scan rates for both perovskite formulations using two different protocols illustrated above related graphs: a) after an initial step of stabilization under light at V_{oc} , a reverse/forward loop is recorded; b) after an initial step of stabilization under light at I_{sc} , a forward/reverse loop is recorded.

The typical patterns of the $J(V)$ curve at four different scan rates for both perovskite formulations are presented in Figure 3 using two different protocols depicted in the columns labeled (a) and (b). The solid lines represent voltage scans in reverse mode (Rev.), while dotted lines represent the forward mode (For.).

As shown in Figure 3a, graphs in the left column were recorded after an initial step of stabilization under light at V_{oc} , followed by a reverse/forward voltage loop between V_{oc} and 0 V. The initial stabilization step is crucial, as it was observed that V_{oc} increased for a few minutes before stabilizing to a reproducible value. Failure to adhere to this step could result

in curves displaying various V_{oc} values depending on whether they were stored in darkness or under light right prior to measurements. This behavior is compatible with a light activation phenomenon recently reported in such devices,^[26,58] and it was observed to be more pronounced for devices with AVAI additive.

Subsequently, as previously described, a common expected curve pattern is observed in the reverse scan at the voltage scan rate boundaries located at 1 mV s^{-1} for lower curve and 500 mV s^{-1} for higher curve. At intermediate levels, a “bump” pattern is observed (here 4 and 40 mV s^{-1} are represented, but the full range of variation is represented in Figure 1).

When following the measurements with a forward scan loop (without interruption between reverse and forward scans), it is also observed that boundary curves present almost negligible hysteresis behavior, which is not the case for intermediate curves. At 4 mV s^{-1} , the forward curve closely resembles the one observed at 1 mV s^{-1} . This means that if this scan speed was initially enough to avoid an immediate interfacial contamination by ion migration (resulting in the “bump” in Rev.), the following For. scan suffered from the final contamination observed after the “bump”. At 40 mV s^{-1} , one can see that once the interfacial contamination has occurred, high scan rates are not well tolerated by the device. Whereas, at higher scan speed ($>500 \text{ mV s}^{-1}$), no interface contamination had time to occur during the complete Rev./For. loop. All these observations are clearly observable for the devices using the formulation with AVAI (top graph in Figure 3a), and are also valid without AVAI (bottom graph in Figure 3a) even if the amplitude is strongly reduced likely due to the difference in cations formulation.

To delve deeper, as shown in Figure 3b, graphs in the right column present $J(V)$ curves recorded following an inverse loop compared to Figure 3a, namely a forward/reverse voltage loop between 0 V and V_{oc} . Similarly, an initial stabilization step was performed, this time at $V = 0 \text{ V}$ (I_{sc} stabilization). However, this did not seem to affect subsequent measurements. In addition, the duration of this stabilization period did not allow for the light activation previously reported when performed at V_{oc} .

Interestingly, low scan speeds (1 and 4 mV s^{-1}) allowed, after the first part of the loop (For. scan), the achievement of the optimized V_{oc} value previously obtained. This suggests that the light activation process can occur as soon as a voltage is applied. The measurement protocol did not affect either the reverse or the forward $J(V)$ curves at 1 mV s^{-1} . In contrast, higher scan speeds (40 and 500 mV s^{-1}) were too fast to permit complete light activation and resulted in lower V_{oc} values. Despite Rev. scans being disadvantaged by lower V_{oc} values for higher scan speeds, the latter allowed reaching higher final J_{sc} values than with lower scan speeds (i.e., devices did not have time to present a complete surface contamination by cation migration). However, the achieved J_{sc} values were lower than with the first protocol. Once again, all observations were clearly observable for the devices using the formulation with AVAI (top graph in Figure 3b), and also valid without AVAI (bottom graph in Figure 3b) with a significantly reduced amplitude.

Sensitivity to moisture and heat is one of the challenges faced by PSCs, including carbon-based perovskite devices.^[37,59] Several studies already highlight the potential of AVAI-based MAPbI₃ formulation to exceed the durability of pure MAPbI₃ perovskite.^[22,25] However, damp-heat comparative aging studies are usually conducted on relatively short duration ($\leq 1000 \text{ h}$, which is the IEC 61 215 requirement for silicon devices) and very few of them are coupled with a study of the mechanisms involved in the difference of lifetime between (5-AVA)_{0.05}MA_{0.95}PbI₃ and MAPbI₃ perovskites. In addition, to the best of our knowledge, no other publication reports the monitoring during 3500 h of PV parameters according to different $J(V)$ measurements conditions. Thus, based on the in-depth above study regarding the impact of measurement conditions, we decided to monitor the PV performances of our C-PSC during aging using both voltage

scan rate boundaries (1 and 500 mV s^{-1}) and scans in reverse mode after an initial step of light activation at V_{oc} . The “bump” pattern generally appears clearly from 4 mV s^{-1} . To avoid it, a low scan speed of 1 mV s^{-1} has been selected, which results in rather long measurement times (20 min , taking into account the 4 min delay for preactivation). In most cases, the “bump” disappears at the initial state with a high scan speed of 100 mV s^{-1} . However, during aging, it was often necessary to increase the scan speed closer to 500 mV s^{-1} to obtain a curve without “bump”. After that, the $J(V)$ curve pattern remains identical when the speed is further increased. **Figure 4** presents the variation of PV parameters for encapsulated C-PSC based on MAPbI₃ perovskite formulated with or without AVAI during an aging campaign conducted under damp-heat conditions ($85 \text{ }^\circ\text{C}$, $85\% \text{ RH}$).

The variation of C-PSCs efficiency for both perovskite formulations, with and without AVAI, is depicted in Figure 4a, with respectively red and blue symbols and lines. The voltage scan rates are delineated as low and high, illustrated by colored dotted and solid lines. Additionally, Figure S3, Supporting Information, presents typical $J(V)$ curves at various voltages for three sampling examples during aging.

First, it is evident that devices containing the perovskite formulation with AVAI exhibit higher performances throughout the aging process. AVAI-based devices present an excellent durability for up to 3500 h , maintaining 50% of their initial performances regardless of the scan speed considered. This could be considered at the level of literature records (see Table S2, Supporting Information, for an overview of damp-heat durability already reported for C-PSCs). Moreover, all PV parameters (J_{sc} , V_{oc} , FF, and $1/R_s$) consistently outperform those of devices without AVAI additive (Figure 4b,d,e,f). Furthermore, the alteration of the $J(V)$ curve with different voltage scan rates persists throughout the aging campaign presented here. We previously reported a similar behavior in a closely related C-PSC architecture at the initial state, which disappeared entirely after 120 h of aging.^[36] In this study, the ZrO₂ layer thickness has been multiplied by three (around $3 \mu\text{m}$ instead of $1 \mu\text{m}$ previously). This modification likely enhances the reservoir for large ionic species between TiO₂ and carbon layer, thereby prolonging its presence until 3500 h .

To provide a more detailed analysis of this phenomenon, Figure 4c presents the differences between the two boundary scan rates for both the envelop areas of the $J(V)$ curve (Δ envelop) and the J_{sc} values (ΔJ_{sc}). First, a consistent trend is observed between Δ envelop and ΔJ_{sc} , except for aging points of devices without AVAI after 3000 h , which should be disregarded. Indeed, there is notably a discrepancy in V_{oc} values obtained after light activation (prior to $J(V)$ reverse scans), indicating a deterioration of devices during the sequence of $J(V)$ measurements, likely due to their nearing end of life state. Taking a close look at delta trends, both perovskite formulations also present similar trends: first, a pronounced decrease until 100 h of aging, followed by slightly oscillating values until 1750 h , a sharp increase around 2000 h , and finally a decline at the end of aging. The initial decrease in the delta between scan rates is due to an initial decrease of all PV parameters except the J_{sc} value at low scan rate, which shows an increase. This suggests a microstructural rearrangement within both solar devices, leading simultaneously to reduced charge extraction and ionic diffusion, evidenced by the

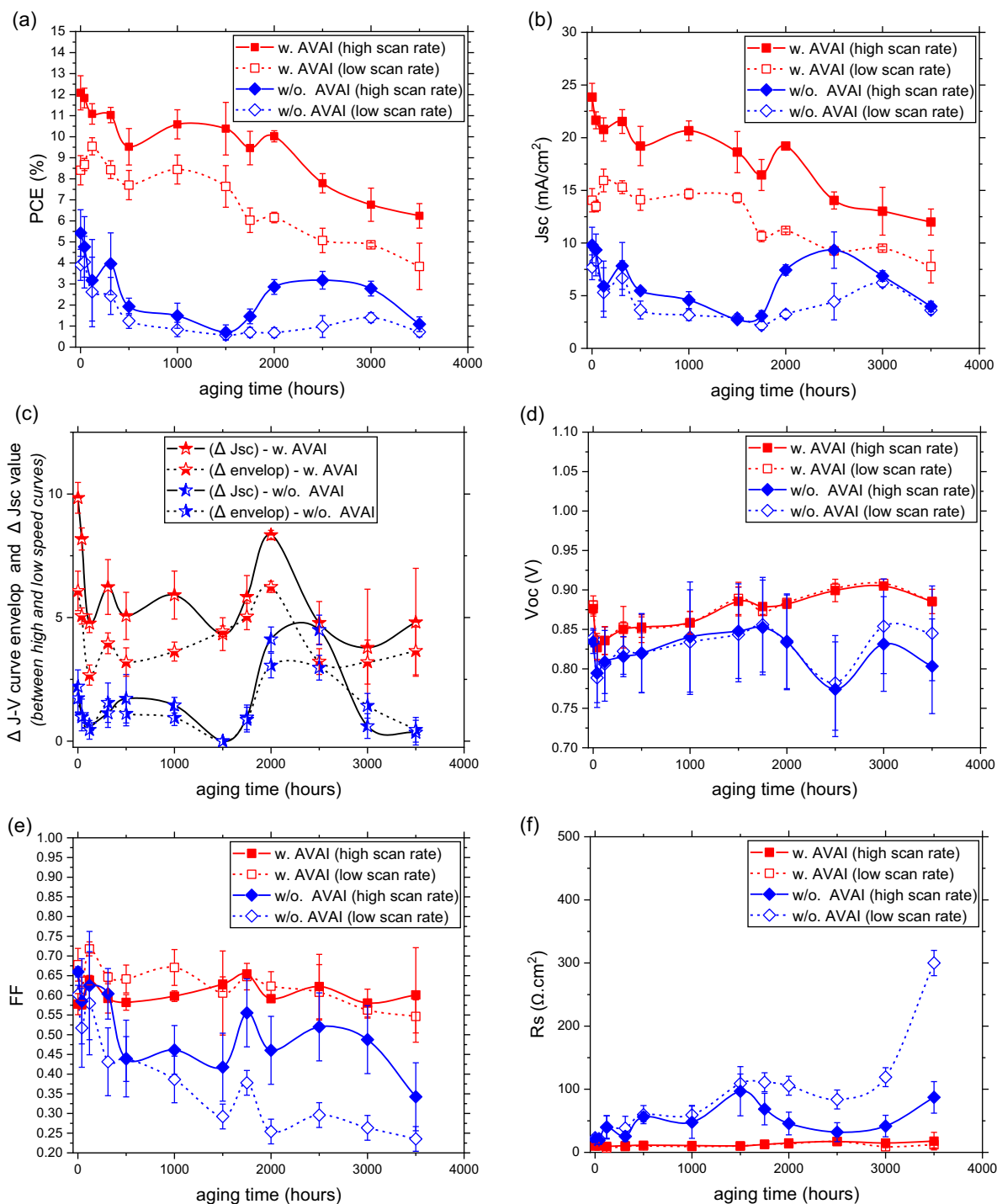


Figure 4. Variations of PV parameters during the 85 °C/85% RH aging campaign for the two studied perovskite formulations: a) power conversion efficiency (PCE); b) short-circuit current density (J_{sc}); c) differences between the two boundaries scan rates for the $J(V)$ envelope areas (mA V cm^{-2}) and the J_{sc} values (mA cm^{-2}); d) open-circuit voltage (V_{oc}); e) fill factor (FF); and f) series resistance (R_s). C-PSCs devices were measured using either 1 mV s^{-1} for low scan rate (empty symbols and dotted lines) or 500 mV s^{-1} for high scan rate (full symbols and full lines).

decrease of J_{sc} for higher scan rates and the increase of J_{sc} for lower scan rates. The notable increase in delta around 2000 h is correlated with a more pronounced increase in J_{sc} for higher

scan rates than for lower ones. It can be here suspected adequate PbI_2 passivation levels,^[60,61] allowing enhanced charge extraction before reaching detrimental levels with further PbI_2

accumulation. Since this occurs at the same aging time regardless the perovskite formulation, it may be due to the onset of water permeation within the encapsulant material.

For C-PSC devices using perovskite formulation with AVAI, their efficiency remains relatively stable until reaching the T80 point at 2000 h (preservation of 80% of initial performance for both scan speed boundaries), after which they undergo a gradual decline, reaching the T50 point at 3500 h. Throughout this aging period, the primary affected parameter is J_{sc} , while other parameters (V_{oc} , FF, and R_s) exhibit minor variations, with V_{oc} returning to its initial values. In contrast, C-PSC devices using perovskite formulation without AVAI exhibit a significant decrease in performance up to 1500 h of aging, accompanied by a decrease in J_{sc} and FF, and an increase in R_s . After 1500 h, devices without AVAI are nearly nonfunctional, with PCE values around 0.6–0.7% reaching T80 before 40 h and T50 before 500 h. However, between 2000 and 3000 h, a huge recovery of PCE occurs, especially at high scan speeds, leading to J_{sc} values returning to levels like those at the initial state for both scan speeds. To understand this particular behavior, we need to recall the presence of an insulating mesoporous zirconia layer between the electron-transport and carbon layers. Due to the requirement of high temperature during the carbon layer process, the perovskite is deposited after the completion of the device backbone stack by drop-casting of the precursors' solution. This requires the addition of an internal insulating mesoporous layer to avoid short circuit. Over time, as the perovskite quantity and/or quality diminished during aging, adequately filling the ZrO_2 mesoporous layer becomes challenging, ultimately leading to the formation of insulating devices. Thus, perovskite devices without AVAI additive undergo a temporary recovery of electrical contact between 2000 and 3000 h thanks to a positive default passivation of the perovskite layer by degradation by-products. However, this punctual recovery zone is surrounded by conditions where devices are almost insulating.

In summary, the perovskite formulation strongly alters the experimental results during aging. Despite having identical architecture, solar cells with AVAI additive exhibit enhanced durability. To better elucidate the degradation mechanisms,

the following study will rely on a full set of characterizations used at different scales of the PV device, from the complete solar cell to the perovskite layer. As a first step, in addition to the conventional $J(V)$ measurements taken throughout the aging tests, imaging techniques were implemented on our devices to provide a more accurate assessment of the local performances.

The LBIC measurement allows for the precise determination of local-induced I_{sc} , offering valuable insight into the spatial distribution of power within a solar cell. Figure 5a presents a sampling of typical LBIC maps obtained during the aging campaign for both type of devices (with or without AVAI), while Figure 5b presents the statistical I_{sc} variation across all sampled points, corresponding to the variations of PV parameters presented in Figure 4.

The initial average LBIC- I_{sc} difference is in perfect agreement with the macroscopic J_{sc} difference observed on $J(V)$ curves performed at low scan rate. Both LBIC- I_{sc} and $J(V)$ - J_{sc} present a multiplicative factor equal to 1.8 between devices without and with AVAI. Then, the average LBIC- I_{sc} evolution closely aligns with the previously examined $J(V)$ measurements at low scan rate. It seems consistent as LBIC measurements conditions are similar to the first point of a forward $J(V)$ scan (Figure 3b), providing a J_{sc} value identical to that of reverse scans at low scan rates (Figure 3a). The alignment of data between $J(V)$ and LBIC is perfect for devices with AVAI all along the aging. For devices without AVAI, the alignment is very close but does not present the recovery behavior observed after 2000 h with $J(V)$. The LBIC- I_{sc} measurements continue to fall and can be assumed equivalent to 0 after 2500 h. This can be due to the significantly lower illumination level using LBIC laser versus the solar simulator, resulting in a diminished generation of charge carriers that could mask the slight recovery observed in electrical contact.

Concerning the LBIC- I_{sc} variation over the full area of devices, it can be noticed a similar level of variation at initial state for both type of device (represented by the uncertainty bar in Figure 5b). During aging, this discrepancy widens for devices with AVAI and diminishes for devices without AVAI. This is attributed to the emergence of a rapidly deteriorated region at the top center of the photoactive layers in well-performing AVAI-based devices,

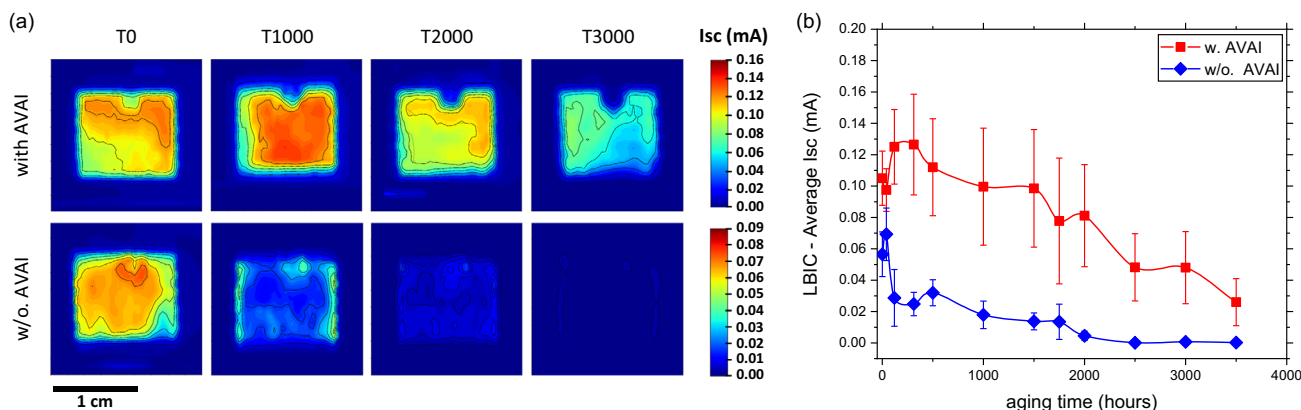


Figure 5. a) LBIC maps of both studied devices for a sampling during the aging campaign (the color scale represents the I_{sc} variation, it was adapted to the type of device as defined by the scale bars on the right of images); b) variation of the LBIC measured average short-circuit current I_{sc} during the aging campaign for perovskite devices with or without AVAI additive (averaged over the active cell area, the uncertainty bar represents the variation over the area of one cell).

which corresponds to the infiltration site of the perovskite precursors' solution. Conversely, for devices formulated without AVAI, the performance decline is uniform across the entire device area.

To correlate the photovoltaic performance of studied devices with the potential degradation of the active layer, we combined the investigations of PV parameters with PL tools. A PL imaging monitoring was performed during the aging campaign for both type of devices (with or without AVAI). **Figure 6a** presents a sampling of typical PL images of the entire active surface area. These PL images were taken from the FTO side of full devices, with the color scale representing the PL intensity ($\mu\text{W cm}^{-2}$) based on a calibration method previously reported.^[62] Imaging is a very useful tool to scout the homogeneity within the full device area. However, to scout potential emission shifts, spectral PL was also performed as presented in Figure 6b for the same sampling examples than PL images.

In PL imaging, a higher emission is evidenced at initial state for devices without AVAI (see average values presented in Figure 6c top graph), consistent with the differences observed in spectral PL (see Figure 2b). The PL images at initial state are rather homogeneous but reveal the infiltration point of the perovskite precursors' solution at the top center. Conversely,

for devices with AVAI, a gradual increase of the average PL is observed throughout the aging campaign. This increase is more pronounced in the center of the cell and at the infiltration point, suggesting a higher density of generated defects. However, defects generated at the center of the cell do not significantly impact PV functional properties, while those at the infiltration point are destructive (see LBIC patterns in Figure 5). It could be hypothesized that the perovskite near the injection point initially contains larger defects, probably due to the formation of larger perovskite crystals initiated before the solution diffusion step, leading to larger voids within the perovskite layer. Despite the overall increase in PL intensity for AVAI-based devices, it remains reasonable compared to devices formulated without AVAI, consistent with the more substantial aging impact on PV efficiency observed in the latter.

Devices without AVAI undergo more pronounced variations during aging, but these variations are more uniform across the entire device. In the first 100 h of aging, MAPbI₃ devices without additive presents a huge PL increase, followed by a progressive decrease until reaching similar average values as devices formulated with the additive. As the initial observed increase of PL is not related to an increase of PCE, we can conclude that it results from an increase of the perovskite layer defects.

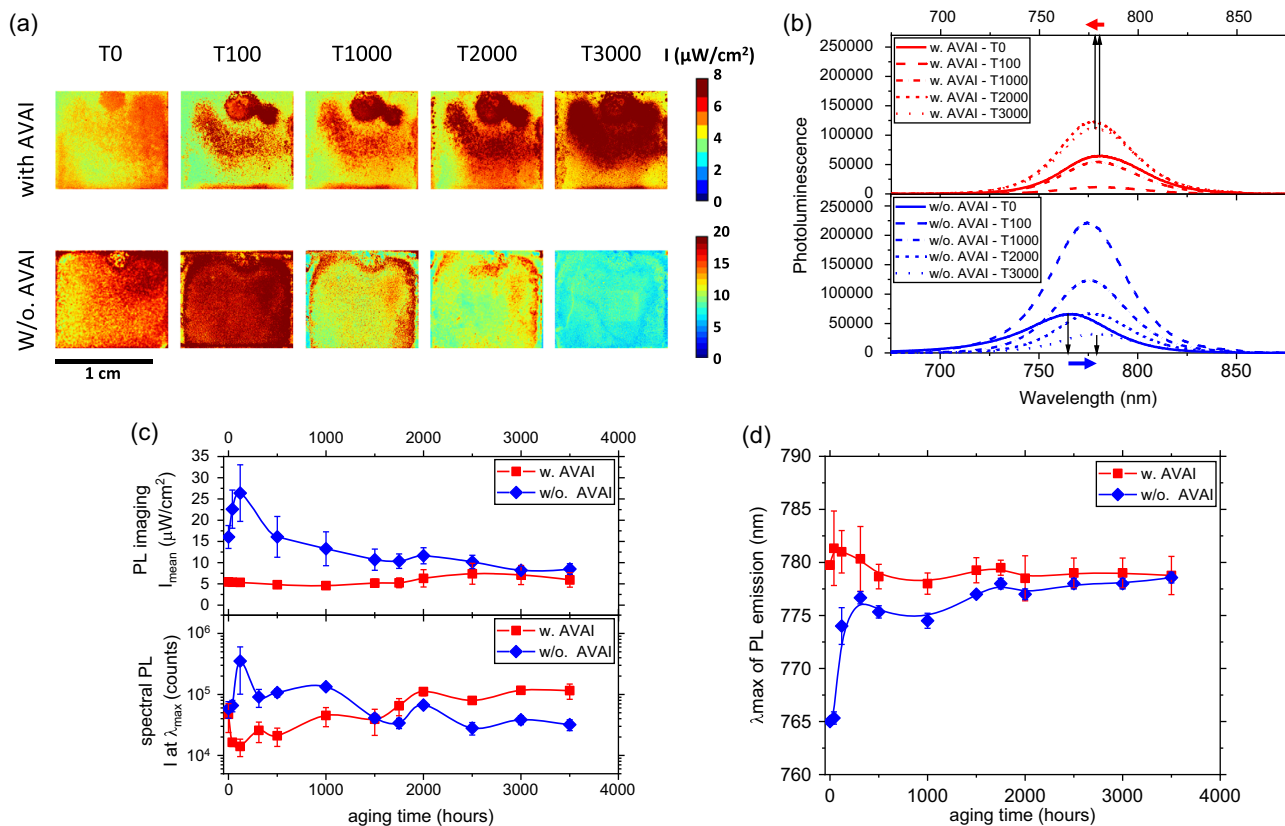


Figure 6. a) PL imaging photos of both studied devices for a sampling during the aging campaign (the color scale represents the PL emission variation, it was adapted to the type of device as defined in the scale bars on the right of images); b) photoluminescence spectra during aging for the same sampling; c) variation during the aging campaign for perovskite devices with or without AVAI additive of (top) the average photoluminescence measured by imaging (averaged over the active cell area, the uncertainty bar represents the variation over the area of one cell) and (bottom) the average spectral photoluminescence measured at λ_{max} (averaged on five cells measurements in the central part, the uncertainty bar represents the standard deviation); and d) wavelength at maximum spectral emission intensity λ_{max} as a function of aging time for both devices.

Nevertheless, this increase is also matching with a non-negligible redshift of the spectral PL emission signal (about 14 nm, see Figure 6b,d). The general trend for strong MAPbI₃ perovskite degradation being a blueshift, a redshift typically indicates an improvement in the crystalline microstructure of the perovskite.^[46] This is further supported by UV–visible spectra (see Figure S2c,d, Supporting Information), where the reflectance level of devices without AVAI decreases during the first 500 h before to increase after 1000 h. As the bandgap amplitude corresponding to perovskite (around 780 nm) also increases, this could be considered as a proof of the perovskite quality enhancement providing an optimization of the absorption during the first steps of the aging campaign. However, as the resulting PCE decreases, other factors also act in parallel. No such variation on UV–visible spectra was observed for devices with AVAI, presenting a very slight initial PL redshift behavior. A PL redshift can be related to several factors, including a decrease in the quantum confinement effect related to an increase of grain size.^[42,50] However, in the mesoporous scaffold considered here, this could also lead to a greater quantity of voids between perovskite crystals, compatible with the observed PL intensity increase and PCE decrease.^[42] Concerning the device with the (5-AVA)_{0.05}MA_{0.95}PbI₃ formulation, a slight PL blueshift trend is observed along the aging. As no final PL blueshift trend was observed for the MAPbI₃ formulation, other type of characterizations like UV–visible spectroscopy and XRD are needed before any conclusion.

Figure 6c also presents the variation of PL intensity obtained from spectral characterization (bottom graph, presented in logarithmic scale), confirming the difference in behavior between the two types of devices. However, a discrepancy between PL imaging and PL spectra emission intensities can be revealed after 1500 h of aging. This could be explained by the fact that the PL spectrometer used only excite a restricted area located in the device central area (about 1 cm high × 1 mm large), whereas AVAI-based devices present a strong inhomogeneity in PL emission intensity within the device area, with a more pronounced emission in the central area scouted using PL spectroscopy.

Here again, it seems useful to investigate further the potential degradation mechanisms within both perovskite active layers (with and without AVAI). UV–visible spectroscopy and XRD analyses will therefore be the subject of the following section. This should help to further interpret PL observations and establish a comprehensive connection with the evolution of PV performances.

Figure 7a,b displays XRD diffractograms during the aging campaign. These analyses are destructive as they necessitate opening the encapsulation and removing a large part of the carbon layer; thus, the sampling was reduced to critical points during the aging campaign. At first glance, the formation and development with aging time of PbI₂ (degradation by-product of perovskite) in its crystalline form can be easily observed for both devices with and without AVAI. This corresponds to a continuous decrease in the perovskite relative crystallinity, as highlighted in Figure 7c. Surprisingly, a much greater proportion of crystalline PbI₂ is observed during the aging of AVAI-based devices while they demonstrate a considerably longer lifespan compared to devices formulated without AVAI. This PbI₂ emergence could be correlated with the high level of PL emission observed in the central area of AVAI-based devices. However,

AVAI-based devices also demonstrate higher levels for the perovskite relative crystallinity than devices without AVAI until end of aging (Figure 7c).

In addition, the appearance of amorphous PbI₂ in sufficient quantity to be observed by UV–visible absorption spectroscopy is demonstrated for devices formulated without AVAI (Figure 7d). A small amount of monohydrated perovskite phase can also be observed by XRD (7.5°–10.5° range).^[63,64] The detected level is within the same order of magnitude for both type of devices and indicates that a slight water permeation through the encapsulant material is already initiated at 1500 h.

Concerning AVAI-based devices, an additional phase around 8.1° is magnified with aging time. According to literature,^[26] this could correspond to the emergence of the 2D perovskite phase in such systems. It thus seems that the degradation of (5-AVA)_{0.05}MA_{0.95}PbI₃ also releases the AVA₂PbI₄ perovskite 2D phase alongside PbI₂, both of which are non-photoactive. It should be mentioned that the release of pure 2D phase could explain the PL blueshift observed with AVAI and not observed without AVAI (Figure 6b,d). Indeed, a reduction of the perovskite atomic distortion initially due to the 2D perovskite phase inclusion could result in a PL blueshift.^[52]

In examining the general pattern of XRD diffractograms, two differences between devices with and without AVAI are notable. First, two signals between 28° and 29° and between 31° and 32° seems to split into different proportions according if devices are with or without AVAI. However, both signals include 2 peaks: one being each time attributed to ZrO₂ (28.2° and 31.5° for respectively the (−111) and (111) planes of monoclinic ZrO₂)^[54] and another attributed to perovskite (28.4° and 31.8° for respectively the (220) and (222) planes of tetragonal MAPbI₃).^[65] The potential splitting^[66] of MAPbI₃ signals in both concerned 2 θ ranges due to the tetragonal structure involved cannot be observed for thin films using our XRD measurement conditions.^[67] For comparison, the XRD diffractogram of ZrO₂/TiO₂/FTO/glass device backbone without perovskite is presented in Figure S2a, Supporting Information.

Second, as the mesoporous structure of TiO₂ allows perovskite to crystallize in various orientations, differences in perovskite orientations were observed between the two systems at the initial state: predominantly orientation 2 for MAPbI₃ and orientation 1 for (5-AVA)_{0.05}MA_{0.95}PbI₃. During aging, both perovskites undergo a degradation/amorphization process. Consequently, for the formulation without AVAI, a strong modification of the perovskite orientations proportions was observed. As illustrated in Figure S2b, Supporting Information, orientation 2 proportion decreased by a quarter to the benefit of orientation 1. Concerning the formulation with AVAI, a quasi-conservation of the perovskite orientations proportions was observed with anyway a slight decrease of orientation 2. The convergence of both perovskite toward a similar orientation proportion after aging suggests that an excessive proportion of orientation 2 may not be conducive to optimal perovskite performance in mesoporous C-PSC architectures and is particularly sensitive to aging effects.

In Figure 7b, both reflectance and absorbance spectra clearly present the bandgap of the 3D MAPbI₃ perovskite near 780 nm. The exact bandgap value for both perovskite formulations (1.58 eV) is not modified during aging, indicating that both residual perovskites after 3500 h of aging are still of good quality,

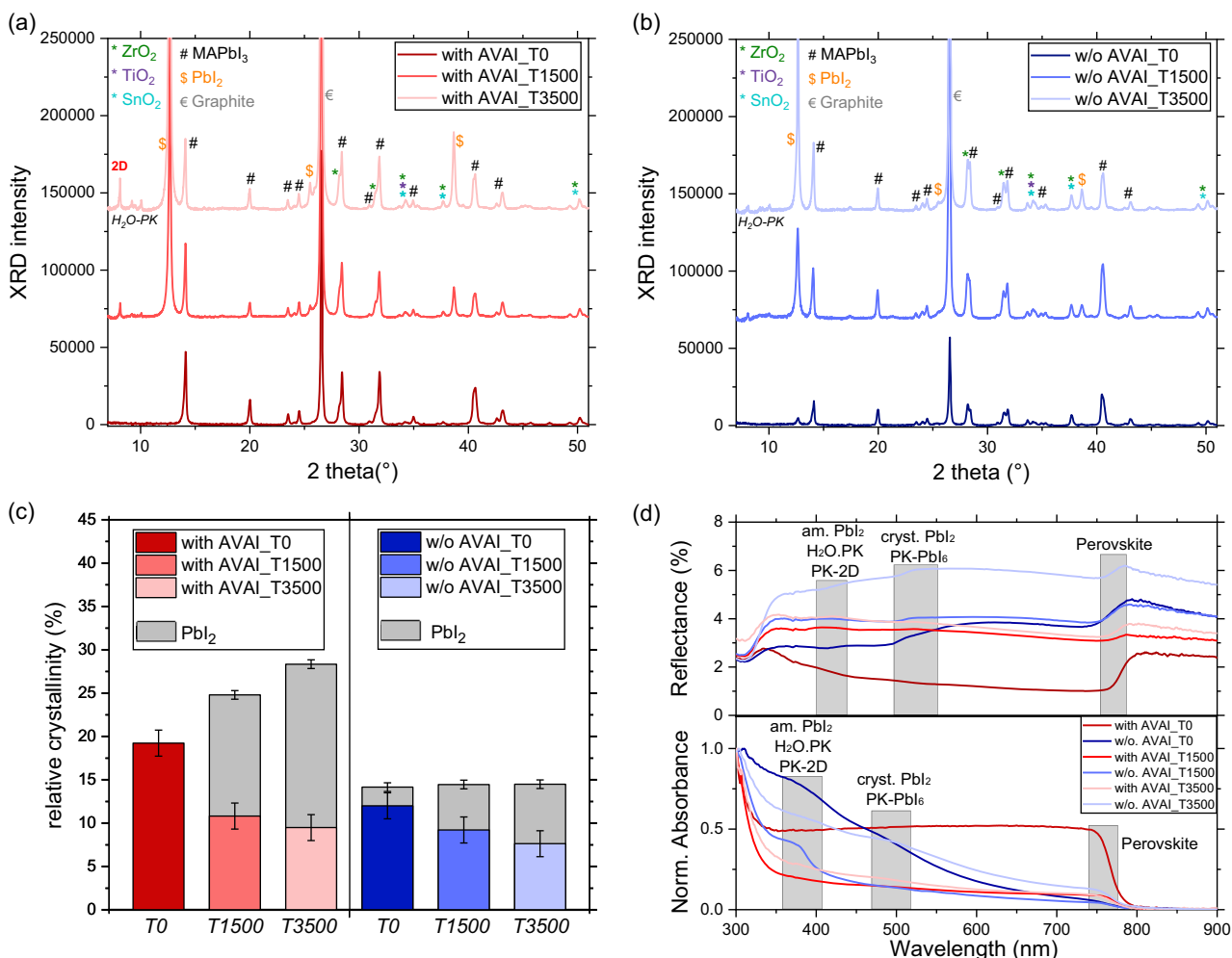


Figure 7. Variations during the 85 °C/85% RH aging campaign of a,b) XRD diffractograms with main diffraction lines assignment (after CL removal) for respectively perovskite layers formulated with and without AVAI; c) XRD relative crystallinity of perovskite (color) and PbI_2 (grey); and d) UV–visible reflectance spectra (performed on complete cells from FTO side) and absorbance spectra (performed on cells after CL removal).

consistent with their relative crystallinity measured using XRD (respectively 9.5% and 7.6% for perovskites with and without AVAI). As reflectance spectra are performed without any alteration of the devices, this characterization can be used to estimate the absorbance level throughout the aging process. At the initial state and throughout aging, reflectance spectra of devices with AVAI are lower than those of devices without AVAI. As the carbon layer avoids any transmission, this allows to conclude that the absorbance level of $(5-AVA)_{0.05}MA_{0.95}PbI_3$ always remains higher than for $MAPbI_3$. This is in accordance with the conservation of better PV performances during aging and highlights the good quality of the $(5-AVA)_{0.05}MA_{0.95}PbI_3$ perovskite layer, even if XRD indicates that its crystallinity rate rapidly converges toward values similar to those of $MAPbI_3$.

Deepening the analysis of obtained UV–visible spectra enables to identify two additional increasing transitions for perovskite without AVAI. The first one, around 500 nm, could correspond to both crystalline PbI_2 and the perovskite lead-iodide octahedra (perovskite– PbI_6). The reduction in range during aging for this

transition (from 490–600 to 500–520 nm, clearly noticeable on reflectance spectra) suggests that the PbI_2 transition predominates over perovskite– PbI_6 , which may be disrupted by perovskite degradation/amorphization and become undetectable. The second transition (between 350 and 450 nm) could correspond to two perovskite degradation by-products: amorphous PbI_2 and monohydrate perovskite.^[40,68]

In the case of the perovskite formulation with AVAI, detecting transitions other than the one corresponding to 3D perovskite near 780 nm is more challenging. However, as XRD indicates these by-products (even at higher levels for crystalline PbI_2), it is inferred that the high level of absorbance of $(5-AVA)_{0.05}MA_{0.95}PbI_3$ perovskite attenuates the visualization of transitions corresponding to white–yellow low-absorbing compounds. Nevertheless, at the end of aging, slight transitions around both 500 and 400 nm become recognizable. The latter may also include the contribution of emerged 2D perovskite.^[22]

After all the characterizations conducted at the perovskite scale, the lower photovoltaic performances and reduced

durability demonstrated by devices formulated without AVAI can be attributed to several factors. These include the observed higher R_s , increased amount of amorphous PbI_2 , higher proportion of perovskite orientation 2, higher UV-visible reflectance level, elevated PL average emission, and lower perovskite crystallinity rate. However, a serious lower quantity of crystalline PbI_2 was also inconsistently observed as compared to $(5\text{-AVA})_{0.05}\text{MA}_{0.95}\text{PbI}_3$ perovskite. It should thus be called to mind that the perovskite layer forms a conductive path within a ZrO_2 insulating mesoporous architecture. Thus, degradation of contacts within the perovskite layer or between perovskite and electrodes can lead to nonfunctional cells, characterized by sudden loss of current. In the present configuration, the combination of $(5\text{-AVA})_{0.05}\text{MA}_{0.95}\text{PbI}_3$ perovskite and PbI_2 does not seem very detrimental before reaching 4000 h, where most devices unfortunately encounter a fall leading to PCE lower than 0.5%. According to literature, PbI_2 passivation of carbon electrode through C–O–Pb linkages allows reducing the recombination due to direct contact between carbon and absorber.^[60] An excess of PbI_2 within the perovskite may not always be detrimental in such architectures and can even lead to beneficial effects by reducing ionic migration or passivating the defects in perovskite grain boundaries.^[69–71] In addition, AVAI-based perovskite is known to possess a potential for better charge extraction at the TiO_2 interface (–COOH adsorbed on both TiO_2 and ZrO_2 mesoporous layers).^[57] These three factors should thus be considered to interpret the superior durability of $(5\text{-AVA})_{0.05}\text{MA}_{0.95}\text{PbI}_3$ perovskite devices.

To conclude, as AVAI additive favors the initial perovskite crystallinity and the PbI_2 degradation by-product in its crystalline form instead of amorphous, the conduction paths through the mesoporous network are maintained for longer when using $(5\text{-AVA})_{0.05}\text{MA}_{0.95}\text{PbI}_3$ formulation perovskite. When the AVAI-based MAPbI_3 starts to release pure AVA_2PbI_4 2D perovskite phase, it means that the remaining level of non-degraded MAPbI_3 perovskite is starting to be a problem. Then, hydrated MAPbI_3 is generated due to leakage of the encapsulation. At 3500 h, the hydrated-perovskite level start to be important in both MAPbI_3 and $(5\text{-AVA})_{0.05}\text{MA}_{0.95}\text{PbI}_3$ formulations. As it could present either 1D or 0D structures for respectively mono- and dihydrate forms,^[72] this is detrimental for the preservation of conduction paths. Even if our devices present an exceptional stability up to 3500 h, the development of encapsulation systems with higher water barrier properties could still conduct to an increase of the C-PSCs stability. Indeed, a recent publication highlights the potential of similar devices to exceed 5000 h of stable PCE under sole thermal stress (85 °C) when properly encapsulated.^[73]

To gain a deeper understanding on mechanisms occurring in both $(5\text{-AVA})_{0.05}\text{MA}_{0.95}\text{PbI}_3$ and MAPbI_3 carbon-based mesoscopic PSCs, impedance spectroscopy measurements were also carried out. Typical Nyquist plots obtained at voltage conditions compatible with real operating conditions are presented in Figure S4, Supporting Information. To analyze the experimental data, the equivalent circuit presented in Figure 8a was used to fit our data. The chosen model includes three resistors and two capacitors that were sufficient to describe the experimental results while also having a physical significance,^[38,74–77] which will be recalled in each of the following related sections.

Figure 8b–f represents the variation with aging time of extracted parameters: respectively R1, C1, R2, C3, and R3. Results were presented using a logarithmic scale for a better visualization of parameters variations.

The R1 resistance represents the Ohmic contributions of contacts. At initial state, R1 is relatively low for both studied systems, measuring 12 and 17 $\Omega\text{ cm}^2$ for devices with and without AVAI, respectively. During aging, this parameter increases in a similar way for the two systems, nevertheless preserving reasonable values until end of aging (respectively 24 and 38 $\Omega\text{ cm}^2$ at 3500 h). Interestingly, a significant increase of R1 is observed around 100 h for both systems, coinciding with their initial observable decrease in PCE. Then, R1 values are relatively stable for AVAI-based devices. Concerning devices without AVAI, R1 value continues to rise with however a significant drop located around the PCE recovery point observable at low scan rate (also noticeable for R2 and R3 resistances).

The sum of R2 and R3 represents the total recombination resistance, R2 being associated with the processes occurring within the active layer and R3 at the perovskite interfaces. Both R2 and R3 resistances increase with a pattern close to the one of R1. However, if initial values are in the same range, the scale of increase is much more pronounced for both R2 and R3 parameters.

At around 100 h of aging, the rise in R3 values is more pronounced than that of R2 value with a factor 10, for both with and without AVAI systems. If we correlate the increase of these recombination processes to PL emission (Figure 6), a direct correlation can be found with the average increase of radiative recombination around 100 h for devices without AVAI. Similarly, for devices with AVAI (although less obvious when considering averaged emission values), careful examination of PL images highlights local points with higher radiative recombination also emerging around the 100 h mark of aging. Given that R3 is much more impacted than R2, it suggests that recombination mechanisms predominantly occur at the interfaces, indicating that the quality of the perovskite interfaces suffers more from created defects than the electrical path created by the perovskite within the insulating ZrO_2 mesoporous layer.

After 100 h, R2 resistance continues its steady growth until the end of aging for both studied systems. This is compatible with the progressive decrease of perovskite crystallinity combined by the increase of degradation by-products. Concerning R3, devices with or without AVAI behave in the same way once again. A large drop of the recombination at the interfaces is evidenced between 100 and 1000 h, likely related to a positive passivation at perovskite interfaces. This allows for the conservation of PCE until 1000 h for $(5\text{-AVA})_{0.05}\text{MA}_{0.95}\text{PbI}_3$ devices. Unfortunately, this was not enough for MAPbI_3 devices, possessing higher R1 and R2 resistances. After 1000 h of aging, all resistances started again a new rise. This was prejudicial for $(5\text{-AVA})_{0.05}\text{MA}_{0.95}\text{PbI}_3$ devices, starting their progressive PCE decrease after 1000 h.

C1 and C3 capacitance show dissimilar behaviors. C1 preponderates at high frequencies and is associated with rapid charge relaxation, it shows the response of the photoactive layer. C3 becomes more noticeable at lower frequencies and results from slower charge movement, indicating charge accumulation at the interfaces resulting in interfacial polarization.

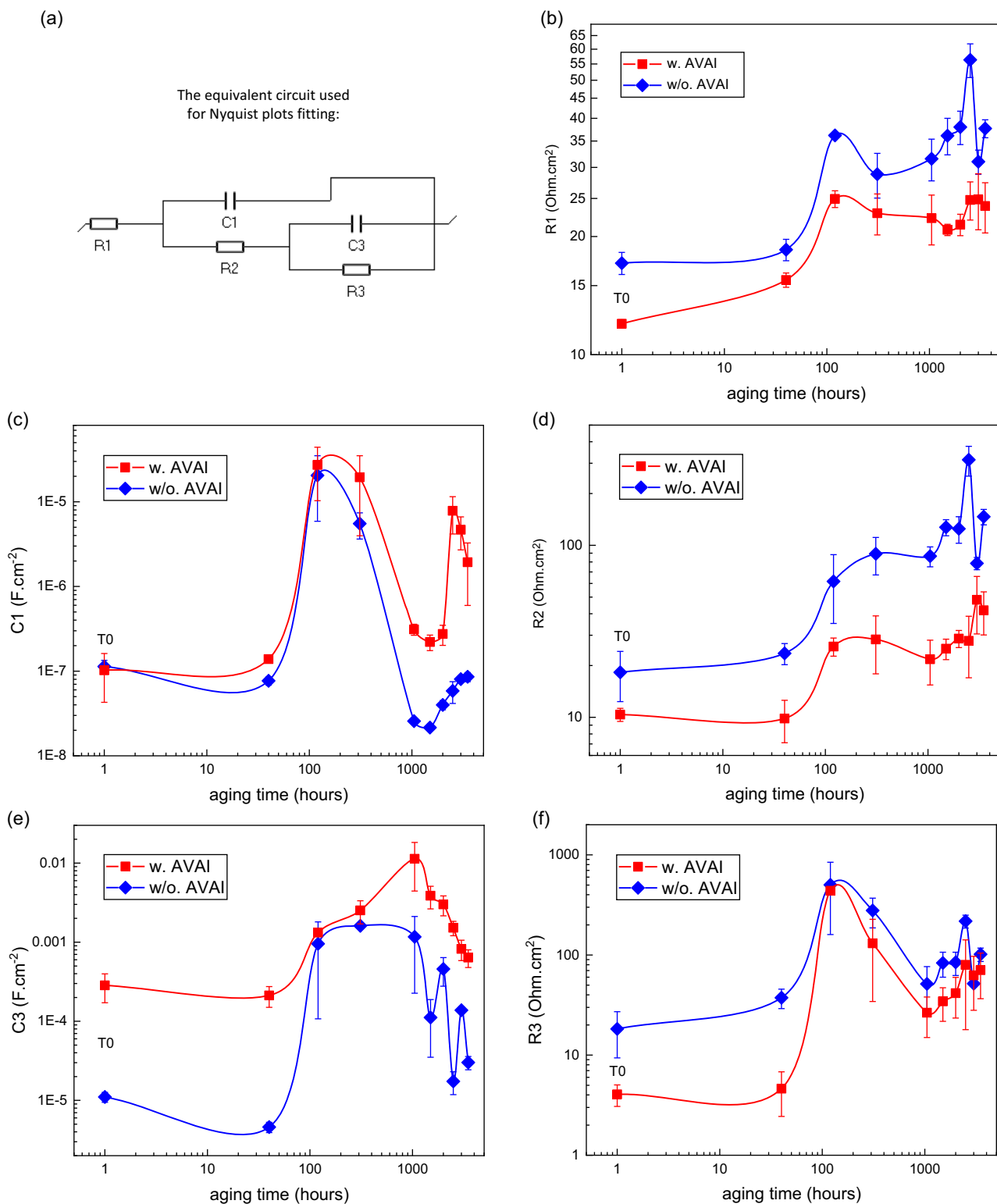


Figure 8. a) Equivalent circuit used for fitting impedance spectra; evolution during aging of parameters extracted from impedance spectroscopy measurements for both studied devices. b,d,f) Resistances ($R1$, $R2$, $R3$) and c,e) capacitances ($C1$, $C2$) under 1 sun in non-open circuit conditions (as results are presented using logarithmic scales, 1 h aging time corresponds to $T0$).

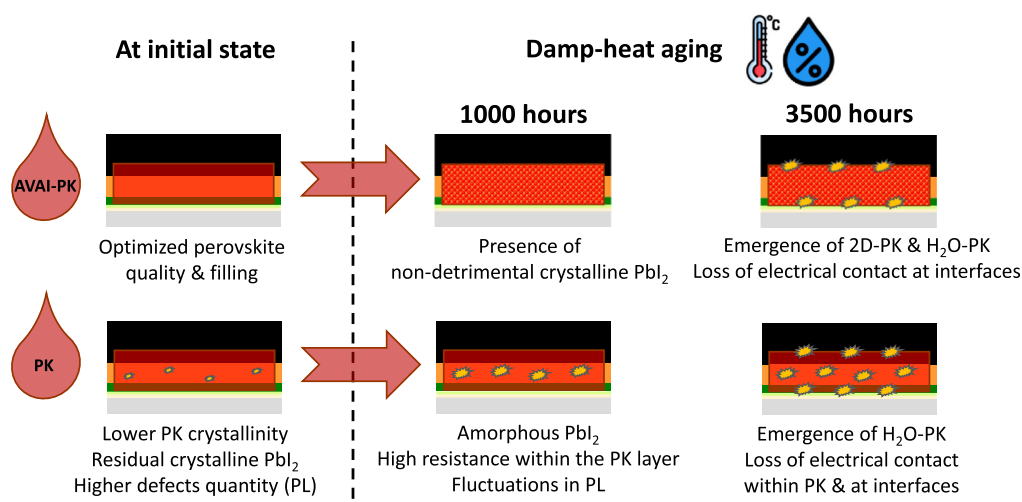


Figure 9. Overview of mechanisms occurring in both studied devices at initial state and during damp-heat aging.

In initial state, the C1 value is equivalent for both studied devices with a value close to $0.1 \mu\text{F cm}^{-2}$. This implies that structural differences between $(5\text{-AVA})_{0.05}\text{MA}_{0.95}\text{PbI}_3$ and MAPbI_3 perovskites do not govern this parameter at the beginning. As the two perovskites present a difference in crystalline orientations proportions, it can suggest that the polarization within the perovskite layer is not the predominant factor reflected by C1. This is in accordance with previous literature observations^[78] and trends to indicate that C1 should be more likely related to an interface within the cell. This seems to be confirmed during aging as the evolution pattern of C1 is then close to the one observed for resistances. However, devices without AVAI present lower C1 values than devices with AVAI. This could be related to the difference of photon absorbance level demonstrated by devices without AVAI, automatically leading to a lower charge generation.

After 100 h of aging, a significant increase of C1 is observed for both devices, corresponding to the first observed drops in PCE, probably due to charge transfer issues at the interfaces or within the perovskite. Between 300 and 1000 h, a significant decrease of C1 is observed. Values obtained for devices with AVAI are again close to initial ones, showing a recovery of the conduction pass through PbI_2 passivation. For devices without AVAI, values are even lower than initial one by a factor close to 10. Although a recovery of the conduction pass within perovskite may also occur, charge accumulation should take place elsewhere, as the PCE of devices without AVAI was quite negligible around 1000 h. However, after 2000 h, C1 parameters increase again indicating charge accumulation within the perovskite, probably due to a too low perovskite crystallinity degree at this aging state for both type of devices.

Concerning C3, the two studied devices present largely different values at initial state (respectively 0.28 and 0.01 mF cm^{-2} for devices with and without AVAI). According to literature,^[74] C3 is mainly associated with a light-induced charge carrier accumulation (holes) near the TiO_2 /perovskite interface, especially for thick perovskite layer such as in our C-PSC device architecture. Thus, as devices with AVAI produce twice more current than devices without AVAI, it could be assumed that the potential

of AVAI-based devices for charge accumulation is greater already at initial stage.

During the first step of aging, C3 values increase for both devices, reaching a similar value at 100 h. According to the simultaneously observed increase of R3 resistance, it is possible to conclude a degradation of perovskite interfaces resulting in a reduction of charge transfer at the interfaces. Until 1000 h, C3 continues to rise for devices with AVAI while remaining quite stable for devices without AVAI. This is attributed to the degradation of both device's perovskite layer, with $(5\text{-AVA})_{0.05}\text{MA}_{0.95}\text{PbI}_3$ beginning to release 2D perovskite, potentially leading to a further decrease in the charge extraction at the TiO_2 interface.

After 1000 h, a general decrease of C3 can be observed for both devices. As meantime C1 increases, this trends to indicate a general degradation of the perovskite (amorphization/degradation by-products) leading to charge accumulation within the perovskite layer itself. Consequently, there are fewer conduction pathways between the perovskite and the electrodes, reducing charge accumulation at the interfaces.

According to impedance spectroscopy characterization, it is thus possible to highlight both a higher perovskite quality within the perovskite itself (R2, C1) and at its interfaces with electrodes (R3, C3) for the formulation using AVAI as additive. The degradation of performance with aging time under damp-heat conditions and at the end of life of C-PSCs devices is related to a different mechanism in devices formulated with or without AVAI. For devices with $(5\text{-AVA})_{0.05}\text{MA}_{0.95}\text{PbI}_3$, the loss of electrical contact predominantly occurs at interfaces (R3 after 1000 h). For devices with MAPbI_3 , it occurs first within the perovskite layer (without AVAI, R1, and R2 levels after 100 h are higher than those of after 1000 h with AVAI), and then at interfaces (R3 after 1000 h). **Figure 9** gives an overview of all occurring mechanisms.

3. Conclusion

A detailed study of correlations among a large series of characterizations (macroscopic PV performances, LBIC imaging, PL

spectroscopy and imaging, UV–visible reflection–absorption spectroscopy, XRD, impedance spectroscopy), conducted both at initial state and as a function of time during damp-heat aging, enabled new insights into the performance and the degradation mechanisms of carbon-based mesoscopic PSCs. The objective of the present study was to focus on the role of AVAI when used as an additive in the MAPbI₃ perovskite formulation. Even if AVAI-based perovskite highlights a higher potential for species diffusion and interface contamination, they also perform better and longer. The (5-AVA)_{0.05}MA_{0.95}PbI₃ formulation perovskite demonstrated a better crystallinity level from the beginning to the end, with a different distribution of the crystalline orientations. This resulted in a highest absorbance of the devices all along aging procedure. In addition, the AVAI-based perovskite possesses a higher ability to produce crystalline PbI₂ than the pure MAPbI₃. The latter one counteracts with amorphous perovskite and amorphous PbI₂. According to impedance spectroscopy, this leads to a loss of electrical contact within the mesoscopic device architecture already at first aging stage for pure MAPbI₃. Indeed, the end-of-life programming of pure MAPbI₃ devices occurs after 100 h of aging with high-resistance levels within the perovskite layer itself (T50 = 500 h), while for (5-AVA)_{0.05}MA_{0.95}PbI₃ devices it occurs after 1000 h with high-resistance levels at the interfaces (T50 = 3500 h).

4. Experimental Section

Materials: All of the following commercial materials were used as received: FTO/glass substrate (TEC-15, Nippon Sheet Glass-Pilkington, Japan), titanium diisopropoxide bis(acetylacetonate) (75 wt% in isopropanol, Sigma-Aldrich, United States), TiO₂ nanoparticle paste (PST-30NRD, JGC Catalysts and Chemicals, Japan), ZrO₂ nanoparticle paste (Solaronix SA, Switzerland), carbon paste (Solaronix SA, Switzerland), methylammonium iodide (Tokyo Chemical Industry, Japan), 5-AVAI (Greatcell Solar, Australia), lead iodide (Tokyo Chemical Industry, Japan), γ -butyrolactone (electrochemical grade, Kanto Chemical, Japan), sealant (thermoplastic ionomer film, PVL0202S, Nisshinbo Mechatronics, Japan).

PV Devices Fabrication and Encapsulation: The carbon-based mesoscopic PSCs (C-PSC) stack configuration consisted of a front FTO/glass substrate with: a compact TiO₂ layer (50 nm) and a mesoporous TiO₂ layer (500 nm) as the electron-transport layers, followed by a 3 μ m mesoporous ZrO₂ insulating layer and a 10–12 μ m mesoporous carbon back electrode. The entire device fabrication process, including the perovskite crystal filling, was performed under ambient air conditions according to procedures previously reported in the literature.^[10,11,58,79–81] The FTO/glass substrate was segmented into small solar cells using a laser etching tool, and the etched substrate was ultrasonically cleaned with a detergent solution (1 wt %, white 7–AL, Yuai Kasei, Japan) for 15 min, followed by ethanol for 15 min. A blocking layer of compact TiO₂ (c-TiO₂) was deposited on patterned substrates by spray pyrolysis deposition of a 0.66 mL titanium diisopropoxide bis(acetylacetonate) solution diluted in 22.5 mL ethanol (1:34 volume ratio). This was carried out on a hot plate at 500 °C with 10 s spray intervals (glass plate masks were placed on electrical contact parts). The thick mesoporous TiO₂ (m-TiO₂) layer was screen printed using a TiO₂ nanoparticle paste, kept for 10 min at room temperature in a container with a lid for leveling, and then dried on a hot plate at 50 °C for 5 min and 140 °C for 5 min. The thick mesoporous ZrO₂ (m-ZrO₂) spacer layer was screen printed using a ZrO₂ nanoparticle paste, kept for 5 min at room temperature in a container with a lid for leveling, and then dried on a hot plate at 50 °C for 5 min and 140 °C for 5 min. The TiO₂ and ZrO₂ layers were then annealed at 500 °C for 1 h in a hot plate with a metal lid (the temperature rise time was 20 min from room temperature to 500 °C and the holding time at 500 °C was 40 min). A thick carbon layer

(m-CL) was then screen printed using a high-temperature carbon paste, kept for 10 min at room temperature in a leveling container with a lid, then dried on a hot plate at 125 °C for 10 min, and finally annealed at 400 °C for 1 h on a hot plate with a metal lid (temperature rise time was 15 min from room temperature to 400 °C and holding time at 400 °C was 45 min). The substrates were then cooled down to room temperature and separated into individual cells before drop-casting 4.0 μ L of the solution containing perovskite precursors on the border of FTO/c-TiO₂/m-TiO₂/m-ZrO₂/m-CL individual mesoscopic stacks (active area = 1.15 cm²). To infiltrate the MAPbI₃ or (5-AVA)_xMA_{1-x}PbI₃ perovskite layers through the mesoporous scaffold, two different perovskite precursor solutions were used. Both consisted of γ -butyrolactone (GBL) as a solvent containing equimolar concentrations (1.2 M) of lead iodide (PbI₂) and methylammonium iodide (MAI). For (5-AVA)_xMA_{1-x}PbI₃ perovskite, 5 mol% of 5-AVAI was added to MAI affording the following precursors formulation: (5-AVA)_{0.05}MA_{0.95}PbI₃. The perovskite layers were then kept at 25 °C for 30 min with a glass-dish cover, annealed at 50 °C for 90 min with a glass-dish cover, and finally 10 min without the glass-dish cover (open air) at 50 °C. As a final step, the PV devices were encapsulated using a cover glass and a thermoplastic ionomer film as a sealant. The sealing film was placed between the cell, covering the entire cell (top and edges). The resulting stacks were laminated at 110 °C for 5 min using a commercial vacuum laminator (PVL0202S, Nisshinbo Mechatronics, Japan).^[26]

Aging Campaigns Conditions: In this article, the so-called damp heat test was used: encapsulated solar cells were aged in a humidity chamber (HCPI50 Memmert, set at 85 °C and 85% RH). Cells were aged in the same orientation as for end-use operating conditions, i.e., transparent FTO electrode side up. Regular sampling of cells was realized to monitor functional, physicochemical, and structural properties. For each perovskite formulation, batches of five PV cells were dedicated to $J(V)$ monitoring and additional cells were used for destructive characterizations.

Characterizations: $J(V)$ measurements were recorded under illumination with a solar light simulator Newport Oriol LCS-100 providing an AM 1.5G spectrum of 1000 W m⁻² light intensity and using a SP-150 potentiostat/galvanostat from Biologic (Software EC-Lab-11.26). The power calibration (1000 W m⁻²) was systematically carried out each day using an Oriol solar meter with a calibrated silicon reference (Model: 91150V—serial number: 801/0871). The light illumination area was 3 × 3 mm (the active area of the device was 1.15 cm², and the mask aperture was 0.09 cm²). For efficiency data collection, the $J(V)$ measurements were performed in reverse mode from open-circuit voltage (V_{oc}) to 0 V using two different scan rates (1 mV s⁻¹ for low scan rate and 500 mV s⁻¹ for high scan rate). Prior to starting measurements, the cells were allowed to stabilize under the solar simulator (between 1 to 4 min until reaching their maximum stable V_{oc} value). The PCE, short-circuit current density (J_{sc}), V_{oc} , fill factor (FF), and series resistance (R_s) parameters were then deduced from $J(V)$ measurements using a home-made Python script in Spyder environment. $J(V)$ profiles at intermediate scan rates and under reverse or forward modes are also presented.

LBIC maps were acquired using a homemade apparatus. It consisted of a 5 mW, 532 nm green monochromatic laser diode including a diaphragm producing a 0.7 mm diameter beam, set on a computer-controlled X–Y moving stage. During scanning of the cell surface, the cell output short-circuit current (I_{sc}) was simultaneously measured by a source measure unit (2602 Keithley, Cleveland, Ohio). Scanning of the whole cell active area took approximately 20 min. Generated current maps were transformed into color scale images using a home-made Python script on Spyder environment, and they were processed via ImageJ freeware (version 1.8.0) for the extraction of both current average values and homogeneity (represented with uncertainty bars) over the full active area of PV cells. It should be mentioned that, due to the laser diameter, a part of the illuminated area was not covered by perovskite when analyzing the last millimeter border, resulting in lower current values which were not considered for average values and homogeneity assignment.

UV–visible diffuse reflectance and absorbance spectra were measured with a Shimadzu UV-2600 spectrophotometer equipped with an integration sphere accessory. Absorbance measurements required a preliminary step of CL removal. Indeed, the opacity of the thick CL layer avoided any

possible transmission of light within the entire device. This was performed using adhesive scotch peeling method and could present the disadvantage of also removing a small quantity of the perovskite layer. In contrast, the measurements in reflectance mode could be performed on the entire solar cell from FTO side, without preparation.

PL spectra were measured with a Shimadzu RF-6000 spectrofluorometer using a 520 nm excitation wavelength on FTO side of full solar cells. A scan rate of 6000 nm min⁻¹, an excitation slit of 5 nm, an emission slit of 5 nm, and a measurement range of 600–900 nm were used. Two filters were added: a 575 nm low-pass in front of the excitation source and a 600 nm high-pass in front of the source of emission to suppress any artifact coming from the spectrophotometer.

PL imaging experiments were performed using a homemade device composed of an opaque chamber with a camera placed 30 cm above the samples and a green light-emitting diode (LED) array with emission spectrum at 525 nm. A 650 nm high-pass filter from Edmund Optics (York, UK) was added to allow for spectral resolution in the setup and to minimize reflection from the excitation LEDs. Full solar cells were observed in the open-circuit condition. The acquisition time was set close to 1000 ms. As the resulting signal varied depending on acquisition conditions (time and gain), not allowing for a direct quantitative comparison of the evolutions observed, a calibration reported in a previous publication allowing for image correction was employed,^[62] allowing to present intensities in W cm⁻². Any additional image treatment (cropping, colorization, or thresholding) was performed with the ImageJ freeware (version 1.8.0).

XRD diffractograms were obtained using a PANalytical X'Pert PRO MPD X-ray diffractometer between 2θ of 7° and 50° with Cu-Kα source. Experiments were performed at Grenoble Consortium of Common Technological Means on opened PV cells (after peeling of CL). XRD patterns were in this article presented after subtraction of the amorphous baseline. In addition, after extraction of the background using Match! software and integration of all diffraction lines (between 10° and 50°), the relative crystallinity of the studied perovskite and the PbI₂ present in the perovskite were evaluated thanks to Equation (1) and (2), as well as the different orientations composing the perovskite layer.

$$\text{Perovskite relative crystallinity (\%)} = \frac{\sum(\text{perovskite contributions})}{\text{Integrated area} - \sum(\text{Contributions other than perovskite})} \times 100 \quad (1)$$

$$\text{PbI}_2 \text{ relative crystallinity (\%)} = \frac{\sum(\text{PbI}_2 \text{ contributions})}{\text{Integrated area} - \sum(\text{Contributions other than PbI}_2)} \times 100 \quad (2)$$

Electrochemical impedance spectroscopy measurements were performed on the full devices (1.15 cm² active area) under solar light simulator Newport Oriol LCS-100 providing an AM 1.5G spectrum and using a potentiostat/galvanostat (SP-300 with impedance measurement option, Biologic), with a potential variation of 30 mV and a range of frequencies between 1 MHz and 0.5 Hz. The measurements were performed under 1 sun of illumination and a voltage of 0.6 V was applied to solar cells. The Nyquist plots ($-\text{Im}(Z) = f(\text{Re}(Z))$) were then studied and fitted by an equivalent circuit using the EC-Lab-11.26 software. Presented results are average results for three monitored devices of each perovskite formulation.

Supporting Information

Supporting Information is available from the Wiley Online Library or from the author.

Acknowledgements

This work has been funded by the “PROPER” international project supported by both the Japan Science and Technology Agency strategic

international collaborative research program (grant no. SICORP 19-191029644) and the French National Centre for Scientific Research (grant no. IRUEC 222437) in the framework of the “EIG Concert Japan” international joint initiative; the “MEL-PERO” international research booster project supported by the French National Research Agency in the framework of the “Investissements d’avenir” program (grant no. ANR-15-IDEX-02); and the European “UNIQUE” project supported under the umbrella of SOLAR-ERA.NET_Cofund by ANR, PtJ, MIUR, MINECO-AEI, SWEA (Cofund ERA-NET Action, N°691664). Authors were also supported by the Savoie Mont-Blanc University yearly AAP. Authors want to thank Dr. Eiji Kobayashi from Kishu Giken Kogyo Co. (Japan), Dr. David Martineau from Solaronix S.A. (Switzerland), and Dr. Simone Mastroianni from Fraunhofer Institute for Solar Energy Systems (Germany) for very fruitful discussions, and the platform of Consortium des Moyens Technologiques Communs (CMTC) of Grenoble INP for laboratory assistance (Thierry Encinas and Stéphane Coindeau).

Conflict of Interest

The authors declare no conflict of interest.

Data Availability Statement

The data that support the findings of this study are available from the corresponding author upon reasonable request.

Keywords

2D/3D perovskites, carbon-based mesoscopic architectures, degradation mechanisms, interfaces, perovskite solar cells

Received: May 28, 2024

Revised: June 30, 2024

Published online:

- [1] A. Kojima, K. Teshima, Y. Shirai, T. Miyasaka, *J. Am. Chem. Soc.* **2009**, *131*, 6050.
- [2] NREL, Best Research - Cell Efficiency Chart, <https://www.nrel.gov/pv/assets/pdfs/best-research-cell-efficiencies.pdf> (accessed: April 2024).
- [3] K. Aitola, G. Gava Sonai, M. Markkanen, J. Jaqueline Kaschuk, X. Hou, K. Miettunen, P. D. Lund, *Sol. Energy* **2022**, *237*, 264.
- [4] S. M. P. Meroni, C. Worsley, D. Raptis, T. M. Watson, *Energies* **2021**, *14*, 386.
- [5] D. Bogachuk, S. Zouhair, K. Wojciechowski, B. Yang, V. Babu, L. Wagner, B. Xu, J. Lim, S. Mastroianni, H. Pettersson, A. Hagfeldt, A. Hinsch, *Energy Environ. Sci.* **2020**, *13*, 3880.
- [6] J. Li, Q. Dong, N. Li, L. Wang, *Adv. Energy Mater.* **2017**, *7*, 1602922.
- [7] L. Fagiolarini, F. Bella, *Energy Environ. Sci.* **2019**, *12*, 3437.
- [8] A. K. Baranwal, H. Kanda, N. Shibayama, H. Masutani, T. A. N. Peiris, S. Kanaya, H. Segawa, T. Miyasaka, S. Ito, *Energy Technol.* **2019**, *7*, 245.
- [9] Z. Ku, Y. Rong, M. Xu, T. Liu, H. Han, *Sci. Rep.* **2013**, *3*, 3132.
- [10] R. Tsuji, D. Bogachuk, D. Martineau, L. Wagner, E. Kobayashi, R. Funayama, Y. Matsuo, S. Mastroianni, A. Hinsch, S. Ito, *Photonics* **2020**, *7*, 133.
- [11] R. Tsuji, K. Tanaka, K. Oishi, T. Shioki, H. Satone, S. Ito, *Chem. Mater.* **2023**, *35*, 8574.
- [12] J. Liu, X. Chen, K. Chen, W. Tian, Y. Sheng, B. She, Y. Jiang, D. Zhang, Y. Liu, J. Qi, K. Chen, Y. Ma, Z. Qiu, C. Wang, Y. Yin, S. Zhao, J. Leng, S. Jin, W. Zhao, Y. Qin, Y. Su, X. Li, X. Li, Y. Zhou, Y. Zhou, F. Ling, A. Mei, H. Han, *Science* **2024**, *383*, 1198.

- [13] M. Stefanelli, L. Vesce, A. Di Carlo, *Nanomaterials* **2023**, *13*, 313.
- [14] D. Bogachuk, P. van der Windt, L. Wagner, D. Martineau, S. Narbey, A. Verma, J. Lim, S. Zouhair, M. Kohlstädt, A. Hinsch, S. D. Stranks, U. Würfel, S. W. Glunz, *ACS Sustainable Resour. Manage.* **2024**, *1*, 417.
- [15] G. Grancini, M. K. Nazeeruddin, *Nat. Rev. Mater.* **2019**, *4*, 4.
- [16] A. Krishna, S. Gottis, M. K. Nazeeruddin, F. Sauvage, *Adv. Funct. Mater.* **2019**, *29*, 1806482.
- [17] I. C. Smith, E. T. Hoke, D. Solis-Ibarra, M. D. McGehee, H. I. Karunadasa, *Angew. Chem., Int. Ed.* **2014**, *53*, 11232.
- [18] A. Mei, X. Li, L. Liu, Z. Ku, T. Liu, Y. Rong, M. Xu, M. Hu, J. Chen, Y. Yang, M. Grätzel, H. Han, *Science* **2014**, *345*, 295.
- [19] H.-S. Choi, H.-S. Kim, *Materials* **2020**, *13*, 3868.
- [20] Y. Hu, Z. Zhang, A. Mei, Y. Jiang, X. Hou, Q. Wang, K. Du, Y. Rong, Y. Zhou, G. Xu, H. Han, *Adv. Mater.* **2018**, *30*, 1705786.
- [21] T. Li, Y. Pan, Z. Wang, Y. Xia, Y. Chen, W. Huang, *J. Mater. Chem. A* **2017**, *5*, 12602.
- [22] G. Grancini, C. Roldán-Carmona, I. Zimmermann, E. Mosconi, X. Lee, D. Martineau, S. Narbey, F. Oswald, F. De Angelis, M. Graetzel, M. K. Nazeeruddin, *Nat. Commun.* **2017**, *8*, 15684.
- [23] D. Zheng, C. Tong, T. Zhu, Y. Rong, T. Pauporté, *Nanomaterials* **2020**, *10*, 2512.
- [24] Y. Hu, S. Si, A. Mei, Y. Rong, H. Liu, X. Li, H. Han, *Sol. RRL* **2017**, *1*, 1600019.
- [25] A. Mei, Y. Sheng, Y. Ming, Y. Hu, Y. Rong, W. Zhang, S. Luo, G. Na, C. Tian, X. Hou, Y. Xiong, Z. Zhang, S. Liu, S. Uchida, T. W. Kim, Y. Yuan, L. Zhang, Y. Zhou, H. Han, *Joule* **2020**, *4*, 2646.
- [26] E. Kobayashi, R. Tsuji, D. Martineau, A. Hinsch, S. Ito, *Cell. Rep. Phys. Sci.* **2021**, *2*, 100648.
- [27] F. Meng, B. Song, T. Dai, X. Li, Y. Yin, Z. Lou, F. Teng, Y. Hu, L. Qin, Y. Hou, *Adv. Funct. Mater.* **2024**, 2402056, <https://doi.org/10.1002/adfm.202402056>.
- [28] X. Li, M. Tschumi, H. Han, S. S. Babkair, R. A. Alzubaydi, A. A. Ansari, S. S. Habib, M. K. Nazeeruddin, S. M. Zakeeruddin, M. Grätzel, *Energy Technol.* **2015**, *3*, 551.
- [29] K. Dileep, *J. Power Sources* **2023**, *559*, 232645.
- [30] K. Fan, Y. Dai, J. Wang, R. Wang, Z. Lu, Y. Lou, G. Zou, *Org. Electron.* **2023**, *117*, 106778.
- [31] P. Holzhey, M. Saliba, *J. Mater. Chem. A* **2018**, *6*, 21794.
- [32] D. V. Anghel, G. A. Nemnes, I. Pintilie, A. Manolescu, *Phys. Scr.* **2019**, *94*, 125809.
- [33] G. De Moor, N. Charvin, C. Farha, T. Meyer, L. Perrin, E. Planes, L. Flandin, *Sol. RRL* **2024**, *8*, 2300998.
- [34] S. Valastro, G. Calogero, E. Smecca, C. Bongiorno, V. Arena, G. Mannino, I. Deretzis, G. Fiscaro, A. La Magna, A. Alberti, *Sol. RRL* **2024**, *8*, 2300944.
- [35] P. Kajal, B. Verma, S. G. R. Vadaga, S. Powar, *Global Challenges* **2022**, *6*, 2100070.
- [36] E. Planes, C. Farha, G. De Moor, S. Narbey, L. Flandin, L. Perrin, *Adv. Mater. Interfaces* **2024**, *11*, 2300849.
- [37] N. Kyranski, L. Perrin, L. Flandin, E. Planès, C. Farha, L. Wagner, K. Sadedine, D. Martineau, S. Cros, *Processes* **2023**, *11*, 2742.
- [38] E. Planes, C. Farha, G. De Moor, S. Narbey, L. Perrin, L. Flandin, *Sol. RRL* **2023**, *7*, 2300492.
- [39] P. Makuła, M. Pacia, W. Macyk, *J. Phys. Chem. Lett.* **2018**, *9*, 6814.
- [40] K. E. A. Hooper, H. K. H. Lee, M. J. Newman, S. Meroni, J. Baker, T. M. Watson, W. C. Tsoi, *Phys. Chem. Chem. Phys.* **2017**, *19*, 5246.
- [41] M. Spalla, L. Perrin, E. Planès, M. Matheron, S. Berson, L. Flandin, *Energies* **2020**, *13*, 1927.
- [42] M. Al Katrib, L. Perrin, E. Planes, *ACS Appl. Energy Mater.* **2022**, *5*, 4461.
- [43] Y. Tian, I. G. Scheblykin, *J. Phys. Chem. Lett.* **2015**, *6*, 3466.
- [44] X. Zhang, J.-X. Shen, W. Wang, C. G. Van de Walle, *ACS Energy Lett.* **2018**, *3*, 2329.
- [45] M. Spalla, L. Perrin, E. Planes, M. Matheron, S. Berson, L. Flandin, *ACS Appl. Energy Mater.* **2020**, *3*, 3282.
- [46] M. Al Katrib, E. Planes, L. Perrin, *Chem. Mater.* **2022**, *34*, 2218.
- [47] A. Merdasa, M. Bag, Y. Tian, E. Källman, A. Dobrovolsky, I. G. Scheblykin, *J. Phys. Chem. C* **2016**, *120*, 10711.
- [48] A. S. Berestennikov, Y. Li, I. V. Iorsh, A. A. Zakhidov, A. L. Rogach, S. V. Makarov, *Nanoscale* **2019**, *11*, 6747.
- [49] J. Von Behren, T. Van Buuren, M. Zacharias, E. H. Chimowitz, P. M. Fauchet, *Solid State Commun.* **1998**, *105*, 317.
- [50] A. Ummadisingu, S. Meloni, A. Mattoni, W. Tress, M. Grätzel, *Angew. Chem., Int. Ed.* **2021**, *60*, 21368.
- [51] D. Hong, J. Li, S. Wan, I. G. Scheblykin, Y. Tian, *J. Phys. Chem. C* **2019**, *123*, 12521.
- [52] G. Liu, L. Kong, P. Guo, C. C. Stoumpos, Q. Hu, Z. Liu, Z. Cai, D. J. Gosztola, H. Mao, M. G. Kanatzidis, R. D. Schaller, *ACS Energy Lett.* **2017**, *2*, 2518.
- [53] L. Dengxue, X. Zhi, M. Xiangchuan, H. Xiaotian, H. Ting, C. Yiwang, *CCS Chem.* **2023**, *5*, 781.
- [54] D. Manoharan, A. Loganathan, V. Kurapati, V. J. Nesamony, *Ultrason. Sonochem.* **2015**, *23*, 174.
- [55] H. Lakhiani, T. Dunlop, F. De Rossi, S. Dimitrov, R. Kerremans, C. Charbonneau, T. Watson, J. Barbé, W. C. Tsoi, *Adv. Funct. Mater.* **2019**, *29*, 1900885.
- [56] S. R. Raga, L. K. Ono, Y. Qi, *J. Mater. Chem. A* **2016**, *4*, 2494.
- [57] A. Pockett, D. Raptis, S. M. P. Meroni, J. Baker, T. Watson, M. Carnie, *J. Phys. Chem. C* **2019**, *123*, 11414.
- [58] R. Tsuji, D. Bogachuk, B. Luo, D. Martineau, E. Kobayashi, R. Funayama, S. Mastroianni, A. Hinsch, S. Ito, *Electrochemistry* **2020**, *88*, 418.
- [59] L. Perrin, L. Flandin, C. Farha, S. Narbey, D. Martineau, E. Planès, *Energies* **2023**, *16*, 5254.
- [60] P. Zhang, G. Kapil, K. Hamada, S. S. Pandey, T. Ma, S. Hayase, *ACS Sustainable Chem. Eng.* **2018**, *6*, 10221.
- [61] T. Du, C. H. Burgess, J. Kim, J. Zhang, J. R. Durrant, M. A. Formation McLachlan, *Sustainable Energy Fuels* **2017**, *1*, 119.
- [62] E. Planes, M. Spalla, S. Juillard, L. Perrin, L. Flandin, *ACS Appl. Electron. Mater.* **2019**, *1*, 2489.
- [63] A. M. A. Leguy, Y. Hu, M. Campoy-Quiles, M. I. Alonso, O. J. Weber, P. Azarhoosh, M. van Schilfgaarde, M. T. Weller, T. Bein, J. Nelson, P. Docampo, P. R. F. Barnes, *Chem. Mater.* **2015**, *27*, 3397.
- [64] J. A. Christians, P. A. Miranda Herrera, P. V. Kamat, *J. Am. Chem. Soc.* **2015**, *137*, 1530.
- [65] X. Guo, C. McCleese, C. Kolodziej, A. C. S. Samia, Y. Zhao, C. Burda, *Dalton Trans.* **2016**, *45*, 3806.
- [66] T. Baikie, Y. Fang, J. M. Kadro, M. Schreyer, F. Wei, S. G. Mhaisalkar, M. Graetzel, T. J. White, *J. Mater. Chem. A* **2013**, *1*, 5628.
- [67] M. Al-Katrib, L. Perrin, L. Flandin, E. Planes, *Adv. Mater. Technol.* **2023**, *8*, 2300964.
- [68] A. Bonadio, L. S. de Oliveira, A. S. Polo, J. A. Souza, *CrystEngComm* **2019**, *21*, 7365.
- [69] V. Kapoor, A. Bashir, L. J. Haur, A. Bruno, S. Shukla, A. Priyadarshi, N. Mathews, S. Mhaisalkar, *Energy Technol.* **2017**, *5*, 1880.
- [70] F. Liu, Q. Dong, M. K. Wong, A. B. Djurišić, A. Ng, Z. Ren, Q. Shen, C. Surya, W. K. Chan, J. Wang, A. M. C. Ng, C. Liao, H. Li, K. Shih, C. Wei, H. Su, J. Dai, *Adv. Energy Mater.* **2016**, *6*, 1502206.
- [71] Y. C. Kim, N. J. Jeon, J. H. Noh, W. S. Yang, J. Seo, J. S. Yun, A. Ho-Baillie, S. Huang, M. A. Green, J. Seidel, T. K. Ahn, S. Il Seok, *Adv. Energy Mater.* **2016**, *6*, 1502104.
- [72] G. H. Imler, X. Li, B. Xu, G. E. Dobereiner, H.-L. Dai, Y. Rao, B. B. Wayland, *Chem. Commun.* **2015**, *51*, 11290.
- [73] R. Tsuji, Y. Nagano, K. Oishi, E. Kobayashi, S. Ito, *Materials* **2024**, *17*, 3002.

- [74] I. Zarazua, G. Han, P. P. Boix, S. Mhaisalkar, F. Fabregat-Santiago, I. Mora-Seró, J. Bisquert, G. Garcia-Belmonte, *J. Phys. Chem. Lett.* **2016**, *7*, 5105.
- [75] A. Guerrero, G. Garcia-Belmonte, I. Mora-Sero, J. Bisquert, Y. S. Kang, T. J. Jacobsson, J. P. Correa-Baena, A. Hagfeldt, *J. Phys. Chem. C* **2016**, *120*, 8023.
- [76] B. Suarez, V. Gonzalez-Pedro, T. S. Ripolles, R. S. Sanchez, L. Otero, I. Mora-Sero, *J. Phys. Chem. Lett.* **2014**, *5*, 1628.
- [77] L. Contreras-Bernal, S. Ramos-Terrón, A. Riquelme, P. P. Boix, J. Idígoras, I. Mora-Seró, J. A. Anta, *J. Mater. Chem. A* **2019**, *7*, 12191.
- [78] L. A. Muscarella, E. M. Hutter, S. Sanchez, C. D. Dieleman, T. J. Savenije, A. Hagfeldt, M. Saliba, B. Ehrler, *J. Phys. Chem. Lett.* **2019**, *10*, 6010.
- [79] D. Bogachuk, R. Tsuji, D. Martineau, S. Narbey, J. P. Herterich, L. Wagner, K. Sugiyama, S. Ito, A. Hinsch, *Carbon* **2021**, *178*, 10.
- [80] T. Shioki, R. Tsuji, K. Oishi, N. Fukumuro, S. Ito, *Photonics* **2024**, *11*, 236.
- [81] S. Ito, R. Tsuji, in *Printable Mesoscopic Perovskite Solar Cells* (Eds: H. Han, M. Grätzel, A. Mei, Y. Hu), Wiley **2023**, pp. 89–104, <https://doi.org/10.1002/9783527834297.ch4>.